THE JOURNAL OF PHYSICAL CHEMISTRY C

Article

Cite This: J. Phys. Chem. C 2017, 121, 22773-22786

pubs.acs.org/JPCC

Adsorption of Aqueous Crude Oil Components on the Basal Surfaces of Clay Minerals: Molecular Simulations Including Salinity and Temperature Effects

J. A. Greathouse,*[,†] R. T. Cygan,[†] J. T. Fredrich,[‡] and G. R. Jerauld[‡]

[†]Sandia National Laboratories, Albuquerque, New Mexico 87185-0754, United States

[‡]BP America, P.O. Box 3092, Houston, Texas 77079, United States

Supporting Information

ABSTRACT: Molecular simulations of the adsorption of representative organic molecules onto the basal surfaces of various clay minerals were used to assess the mechanisms of enhanced oil recovery associated with salinity changes and water flooding. Simulations at the density functional theory (DFT) and classical levels provide insights into the molecular structure, binding energy, and interfacial behavior of saturate, aromatic, and resin molecules near clay mineral surfaces. Periodic DFT calculations reveal binding geometries and ion pairing mechanisms at mineral surfaces while also providing a basis for validating the classical force field approach. Through classical molecular dynamics simulations, the influence of aqueous cations at the interface and the role of water solvation are examined to better evaluate the dynamical nature of cation−organic complexes and their coadsorption onto the clay surfaces. The extent of adsorption is controlled by the hydrophilic nature and layer charge of the clay mineral. All organic species studied showed preferential adsorption on hydrophobic mineral surfaces. However, the anionic form of the resin (decahydro-2-naphthoic acid), expected to be prevalent at near-neutral pH conditions in petroleum reservoirs, readily adsorbs to the hydrophilic kaolinite surface through a combination of cation pairing and hydrogen bonding with surface hydroxyl groups. Analysis of cation−organic pairing in both the adsorbed and desorbed states reveals a strong preference for organic anions to coordinate with divalent calcium ions rather than monovalent sodium ions, lending support to current theories regarding low-salinity water flooding.

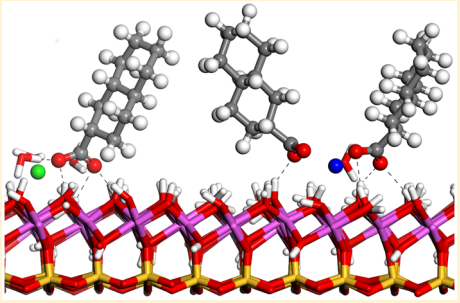

1. INTRODUCTION

Since the work of Tang and Morrow,[1] there has been a mounting number of empirical observations that oil recovery is improved by lowering the salinity of injected brines. There has been much subsequent work and interest to further study and elucidate the underlying reason for the experimental observations so that reliable predictions when such an effect will occur can be made. The current hypothesis for the mechanism that drives this salinity effect is based on the role of cation exchange at clay mineral surfaces in liberating incremental oil. In laboratory-scale core floods and during field tests, oil recovery is enhanced when the chemistry of the invading water is selectively modified.[2,3] Divalent cations such as Ca^{2+} and Mg^{2+} are thought to bind organic molecules through one or more of the following multicomponent ion exchange (MIE) mechanisms: cation bridging, ligand bridging, water bridging, and van der Waals interactions.[4,5]

Additional insight into the molecular processes involved in low-salinity water flooding is needed to determine the relevance of MIE processes at the oil−mineral interface. At the higher level of theory, quantum calculations have been used to investigate the role of cation bridging in the adsorption of small organic acids on mineral surfaces.[6] Classical molecular simulation has also been used to investigate MIE processes for much larger model systems and under a variety of physical and chemical conditions.[5,7,8] Recently, Underwood et al.[5] used molecular dynamics (MD) simulation to investigate surface interactions governing the adsorption properties of a hydrocarbon (decane), and its carboxylic acid/anion variants, on charged surfaces of Na- and Ca-montmorillonite. Possible MIE mechanisms were explored by varying the solution salinity and protonation state of decanoic acid.[5]

Although similar in spirit to the aforementioned work, in this study we include an expanded set of organic species, mineral surfaces, and temperatures to explore the role of hydrophobic and hydrophilic interactions at mineral−fluid interfaces relevant to enhanced oil recovery. Specifically, multiscale molecular simulation is used to investigate the adsorption of representative organic molecules common to crude oil on the basal surfaces of three representative clay minerals: kaolinite, pyrophyllite, and Ca-montmorillonite. Quantum calculations using density functional theory (DFT) are performed on dry surfaces to determine the optimal nuclear and electronic geometries through minimization of the system potential

Received: June 30, 2017
Revised: September 15, 2017
Published: September 28, 2017

DOI: 10.1021/acs.jpcc.7b06454
J. Phys. Chem. C 2017, 121, 22773−22786

energy, as demonstrated on endmember clay minerals.[9] Classical MD simulation allows the effects of explicit solvent and temperature to be included, but at a lower level of theory than DFT. Through MD simulation, trends in adsorption properties are investigated as a function of clay mineral surface, adsorbate properties, and ionic strength. Simulations were performed at room temperature and a higher temperature (366 K) more common to petroleum reservoirs. Our MD approach combines well-known force fields for organic molecules (CVFF)[10] and clay minerals (Clayff)[11] and is validated by comparing geometric properties of surface complexes with DFT. Different initial solute configurations are used to investigate the effect of surface complexes (e.g., water bridging, cation bridging) on resin adsorption.

In addition to the structure, composition, and layer charge of clay minerals, crystal morphology has an impact on adsorption phenomena. Exposure of surfaces to fluids, both oil and aqueous phases, is controlled by the crystal habit, or morphology, of the clay mineral. Basal surfaces usually dominate the effective surface area of most 2:1 clays like smectite and illite, while the edge surfaces have a more significant role in controlling adsorption onto kaolinite.[12] Additionally, acid−base reactions dominate edge sites of clay minerals, and, therefore, solution pH will control the extent of adsorption, especially for charged adsorbate species. This is a more complicated situation that is technically challenging, so only pH-independent basal surfaces are included here, although simple protonation schemes involving the edges of clay minerals are gradually being implemented into classical molecular dynamics simulations.[13−18]

2. MODELING METHODS

The chosen clay minerals are endmember cases and include the fundamental structure of the characteristic layer and sheet topologies found in most natural clay minerals. The minerals are selected to represent the two alternative clay mineral configurations, i.e., one tetrahedral and one octahedral sheet coordinating in each layer (1:1) or two tetrahedral sheets sandwiched about one octahedral sheet (2:1), and with different charge, shown in Figure 1 and discussed below.

Kaolinite, $Al_2Si_2O_5(OH)_4$, is a charge-neutral 1:1 clay, consisting of one $AlO_2(OH)_4$ octahedral sheet and one SiO_4 tetrahedral sheet, with no exchangeable cations. The octahedral and tetrahedral sheets form aluminol and siloxane basal surfaces, respectively. Adsorption onto the aluminol surface will be examined since the siloxane surface is similar to that of pyrophyllite (see below). A combination of van der Waals and hydrogen bond interactions may still allow adsorption of neutral or charged organics. Although natural kaolinite minerals contain trace impurities that result in a small exchange capacity and could enhance the adsorption of weakly interacting organic species, the initial work presented here includes only pure kaolinite compositions and basal surfaces.

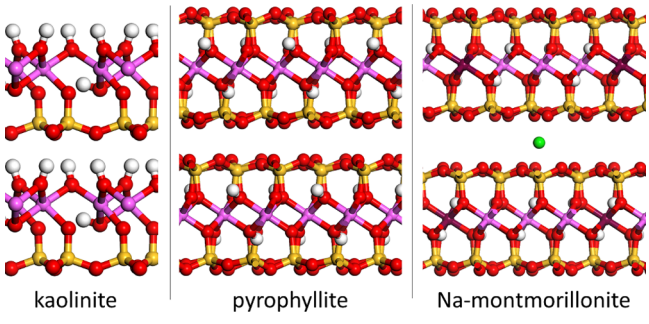

Figure 1. Basic molecular structures of the three clay minerals in this study. Atoms are colored Si (yellow), Al (light purple), O (red), H (white), Mg (dark purple), and interlayer Na^+ (green). This color scheme is used for subsequent figures.

Pyrophyllite, $Al(Si_2O_5)(OH)$, is a charge-neutral 2:1 clay (one octahedral sheet sandwiched between two tetrahedral sheets) with no exchangeable cations. It is an endmember clay that will be used to compare crude oil molecule adsorption with other 2:1 clay minerals that possess layer charge. The basal siloxane surfaces of pyrophyllite are known to be hydrophobic, and the effect of this hydrophobic surface on adsorption will also be compared.[19]

Smectites are negatively charged 2:1 clays with exchangeable cations such as Na^+ or Ca^{2+}. The permanent negative charge is due to isomorphic cation substitution in either the tetrahedral or octahedral sheets.[20] Smectites are classified according to the magnitude and location of the negative charge. For this study, only montmorillonite is considered, which contains negative charge primarily in the octahedral sheet. For the DFT calculations, both Na^+ and Ca^{2+} will be considered exchangeable cations, particularly since Ca^{2+} is common to natural clays, and due to the envisioned role played by divalent cations in proposed MIE mechanisms during water flooding. For the classical MD simulations, only Ca-montmorillonite is modeled, although both Na^+ and Ca^{2+} are present in the aqueous regions in contact with external basal surfaces. The montmorillonite model contains a layer charge of −0.75 e per unit cell with a unit cell formula $M_x[Si_8][Al_{3.25}Mg_{0.75}]O_{20}(OH)_4$, where the brackets containing Si and Al refer to tetrahedral and octahedral sheets, respectively, and M_x refers to the exchangeable cation ($Ca_{0.375}$ and $Na_{0.75}$).

Crude oils are a continuum of tens of thousands of different hydrocarbon molecules, even though the proportions of the elements vary over fairly narrow limits.[21] Nevertheless, a wide variation in properties is found from the lightest crude oils to the highly asphaltenic crude fractions. The carbon content normally is in the range 83−87%, the hydrogen content varies between 10% and 14%, and varying small amounts of nitrogen, oxygen, sulfur, and metals (Ni and V) are also present. Owing to the complex composition of crude oils, characterization by individual molecular types is generally not possible, and hydrocarbon group type analysis is commonly employed. One such analysis defines four "SARA" fractions, saturates (S), aromatics (A), resins (R), and asphaltenes (A), based on differences in solubility and polarity.[21] While the polar fractions, the resins and asphaltenes, are the implicated parties in the MIE mechanism, the nonpolar saturates and aromatics will be considered as a validation of the modeling approaches.

A nonpolar straight-chain alkane (hexane) and a nonpolar cyclic alkane (cyclohexane) represent saturates, while toluene is considered as a representative lightweight aromatic. Decahydro-2-naphthoic acid, DHNA,[22] is examined as a representative resin (Figure 2). Although resin molecules such as DHNA should exist in the deprotonated anionic form at the intermediate pH values of most petroleum reservoirs,[23] both protonated and deprotonated forms will be included here. In the case of the deprotonated carboxylate, a sodium ion is included in the aqueous region to balance the negative charge of $DHNA^-$.

DOI: 10.1021/acs.jpcc.7b06454
J. Phys. Chem. C 2017, 121, 22773−22786

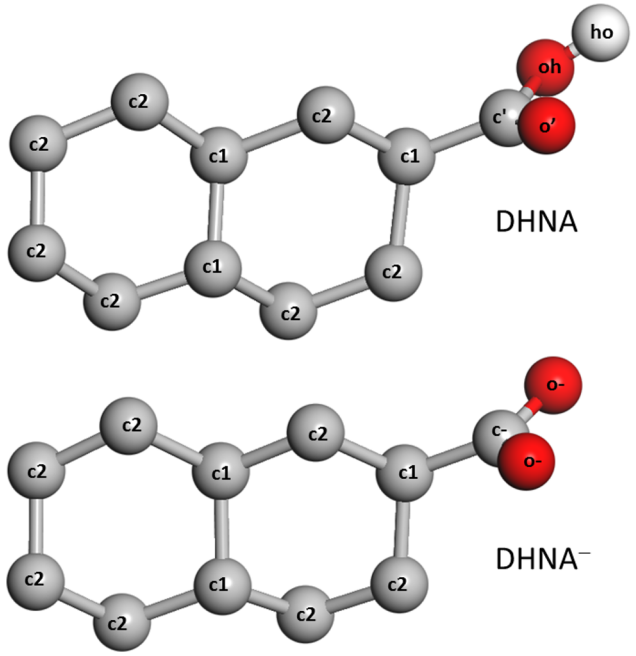

Figure 2. Chemical structures of the resin (decahydro-2-naphthoic acid) used in this study. Atoms are labeled by their CVFF atom types.

2.1. DFT Methods. The model system for DFT calculations involves a periodic supercell consisting of two to four unit cells of clay mineral and one adsorbate crude oil molecule. The DFT simulations provide a very detailed electronic structure description of the bonding environment between adsorbate molecules and clay mineral surfaces. The effects of adsorbed water molecules are not included due to the large computational cost of such systems. Nonetheless, these results provide a rigorous basis for developing the more pertinent large-scale systems using classical simulation methods discussed below. Optimized all-electron configurations were obtained for the selected systems using the DMol[3] software[24,25] and the generalized gradient approximation using GGA(PW91) functionals[26] and the Gaussian double-ζ plus polarization function (DNP) basis set. Calculations were performed at the gamma point with a SCF convergence criteria of 1.0×10^{-5}. Iteration of the wave equations to a self-consistent field solution was used to obtain accurate potential energy values and ultimately to derive binding energies through a comparison of the isolated and associated molecular models. Optimized all-electron configurations were derived for the gas-phase organic compound, slab model representations of the basal hydroxyl surface of kaolinite and the basal surfaces of pyrophyllite and Ca-montmorillonite, and the adsorbed organic on each of the surfaces. Details of the DFT simulation cells for each of the three clay mineral substrates are given in Table 1.

Initial structures for kaolinite and pyrophyllite were taken from published crystal structures,[27,28] and the full crystallographic symmetry was maintained. Since no single crystal structure exists for montmorillonite, an orthogonal unit cell created from the pyrophyllite structure was used for ease of construction and computation. The slab models used in the DFT calculations were created by expanding the unit cell of kaolinite, pyrophyllite, and montmorillonite to provide a sufficient surface area for the unhindered adsorption of the organic molecule, and a vacuum gap of 20 Å above the clay surface that was large enough to avoid any interaction of the organic molecule with the opposing periodic surface. The kaolinite and pyrophyllite models represent uncharged clay surfaces. The montmorillonite model has zero net charge but possesses layer charge created by the substitution of magnesium for octahedral aluminum. The charge is internally compensated by interlayer calcium ions that are disposed on the opposing surface of the montmorillonite. Sodium or calcium ions were introduced in several of the simulations to examine the competition between the organic and metal for a particular binding site and to assess any adsorption enhancement that the metal provides bridging the organic to the clay surface. Additional DFT calculations were performed for isolated cations and several cation−organic complexes.

All atomic positions were allowed to vary during the optimization of each of the molecular systems, while the cell volume was fixed based on the cell parameters derived from previous classical simulations. During the optimization, iteration of the wave equations to a self-consistent field solution required an energy difference of less than 0.0063 kcal·mol^{-1}. Energy minimized structures were derived through a series of steepest descent, conjugate gradient, and Newton−Raphson methods allowing all atoms to relax during the optimization. An energy convergence criteria of 0.013 kcal·mol^{-1} was used for the geometry optimization. Maximum force (2.51 kcal·mol^{-1}·Å^{-1}) and maximum displacement (0.005 Å) criteria were also met for all but one of the reported optimized structures.

A total of 38 separate DFT geometry optimizations were performed to obtain the lowest energy configuration for each molecular system. Each optimization involves the iterative self-consistent field solution to the DFT equations for each step of the geometry optimization. Depending on the initial configuration of the molecular system, the geometry optimization process varied from only a few iterations to as many as eighty-two iterative steps. It was often necessary to reevaluate the optimized configuration using a new initial configuration to ensure the attainment of a global energy-minimized structure. Select interatomic distances from the DFT-optimized structures are provided in the Supporting Information (Tables S1−S4). For select DFT models, corresponding geometry optimization calculations were performed using the Forcite module of Materials Studio (Biovia, Inc.), with the same force field parameters as described in the MD methods below.

2.2. MD Methods. MD simulations using the LAMMPS code[29] were used to derive the structural properties of clay−

Table 1. Formulas, Cell Lengths (Å), and Cell Angles (deg) of Clay Minerals Used in the DFT Calculations

clay mineral	# atoms	*a*	*b*	*c*	*α*	*β*	*γ*
kaolinite	272	20.5960	17.8680	27.3840	91.93	105.04	89.79
pyrophyllite	320	20.6398	17.9320	26.6628	91.18	100.46	89.64
Ca-montmorillonite[a]	323	20.8316	17.9078	27.9227	90.00	90.00	90.00

[a]An orthogonal cell was used for Ca-montmorillonite calculations.

DOI: 10.1021/acs.jpcc.7b06454
J. Phys. Chem. C 2017, 121, 22773−22786

Table 2. Mineral Formulas, Cell Dimensions, and Aqueous Phase Compositions for MD Simulations

	kaolinite	pyrophyllite	Ca-montmorillonite
unit cell[a]	$[Si_4][Al_4]O_{10}(OH)_8$	$[Si_8][Al_4]O_{20}(OH)_4$	$Ca_{0.375}[Si_8][Al_{3.25}Mg_{0.75}]O_{20}(OH)_4 \cdot (H_2O)_8$
supercell ($a \times b \times c$)	8 × 5 × 3	8 × 4 × 3	8 × 4 × 2
lattice parameters[b]	41.6 × 44.7 × 21.5	41.7 × 35.9 × 27.9	41.5 × 35.9 × 29.4
surface area[c]	1860	1490	1490
aqueous phase[d]			
water	1550	1248	1500
cyclohexane	22	17	17
N-hexane	16	13	13
toluene	22	17	17
DHNA/DHNA$^-$	14	12	12
ppm of $CaCl_2$[e]	0	0	0
	645	801	801
	1290	1602	1602

[a]The first and second bracketed terms refer to ions in the tetrahedral and octahedral sheets, respectively. [b]Lattice parameters in Å obtained from constant-pressure MD simulations at 300 K. [c]Areas in Å^2 of the basal surface (*ab* plane). [d]Numbers of water and organic species in aqueous region. Only one organic species was included in each simulation. [e]Effective $CaCl_2$ concentrations from addition of one or two Ca^{2+} and accompanying Cl^- to the aqueous phase.

adsorbate surface complexes and the partitioning of solute species between the diffuse and adsorbed layers at the mineral–fluid interface. We have applied this simulation method to aqueous actinide adsorption onto clay surfaces,[30−32] and the extension to organic solute is straightforward. Additionally, comparison of classical and DFT structures and binding energies provides a strong validation basis for the energy force field and the comparison of thermodynamic properties.

Supercells of each mineral phase were created from crystal structures of kaolinite[27] and pyrophyllite,[28] and orthogonalized for ease of computation and analysis. The Ca-montmorillonite structure was created from the pyrophyllite model by substituting Mg for Al in the octahedral sheet to generate a permanent layer charge of −0.75 *e* per unit cell, as described previously.[33] The composition of each mineral phase and optimized supercell parameters from constant-pressure simulation (details described below) are given in Table 2. As nonswelling clay phases, kaolinite and pyrophyllite models were created without interlayer water or layer charge. Water molecules and Ca^{2+} ions were included in the interlayer of Ca-montmorillonite, which bears a net negative charge.

Force field parameters for the mineral phases were taken from Clayff,[11] which has been shown to accurately reproduce bulk properties of dry and hydrated clays[9,33−41] as well as interlayer and interface properties.[19,30−32,42−45] Clayff incorporates the flexible SPC water model[46] and validated cation potentials.[47,48] We consider organic solutes representing three components of crude oil: two saturates (*n*-hexane, cyclohexane), an aromatic (toluene), and a resin (DHNA) in both protonated and deprotonated forms. Each DHNA$^-$ anion was accompanied by a sodium ion for charge balance. Force field parameters for the organic species were taken from the consistent valence force field (CVFF),[10] a general purpose force field for organic molecules. Clayff uses the same analytical expressions for the potential energy as CVFF, so parameters from both force fields can be combined for hybrid organic–inorganic systems. Recent simulations of ethylene glycol interactions with clay mineral surfaces showed that the combination of Clayff and CVFF compared favorably with other hybrid force field approaches and X-ray diffraction.[49] Force field parameters for all organic species are provided in the Supporting Information.

Starting from the optimized bulk mineral structures, aqueous regions approximately 30 Å thick were created and filled with water molecules and an appropriate number of a single organic species. The number of each organic species in Table 2 corresponds to approximately half-monolayer coverage on each surface. The formation of oil–wet clay surfaces upon excess adsorption, or the aggregation of organic solute in the aqueous phase, would require larger model systems with a greater concentration of organic solute. Only adsorption onto the hydroxylated basal surface of kaolinite was considered since the siloxane surface is analogous to the pyrophyllite basal surface. Ionic strength effects were included by adding one or two calcium ions and accompanying chloride ions to each aqueous phase.

Constant-volume MD simulations of each mineral-solution system were performed at thermostat temperatures of 300 and 366 K with a relaxation time of 100 fs. For constant-pressure simulations of bulk mineral phases, a barostat pressure (0 bar) was used with a relaxation time of 500 fs. Slab boundary conditions were used such that three-dimensional periodic boundary conditions were applied, while a vacuum gap equal to 3*c* prevented short- or long-range interactions between adjacent images in the vertical *c*-direction. The slab boundary condition also prevented the aqueous phase from interacting with the periodic image of the clay surface, so only one mineral–solution interface was simulated. Short-range interactions were evaluated every 0.5 fs, and long-range electrostatic interactions were evaluated every 1.0 fs with a particle–particle particle–mesh (PPPM) summation algorithm[50] with a precision of 1.0×10^{-4}. The aqueous region was terminated by a hard wall to prevent the escape of water molecules into the vacuum region.

For each mineral–solution system, a set of 20 initial configurations were created from a 0.2 ns simulation at 1000 K. At this elevated temperature, the organic molecules move randomly about the aqueous region because their thermal energy is sufficient to overcome regions of attraction at the clay surface (Figure 3). We are confident that this approach removes any bias toward initial configuration. The 20 initial configurations were cooled to the desired temperature (300 or 366 K) and simulated for 4.0 ns. Data from the final 2.0 ns of simulation time were analyzed, and adsorption data were averaged over all 20 simulations. Throughout the MD

DOI: 10.1021/acs.jpcc.7b06454
J. Phys. Chem. C 2017, 121, 22773−22786

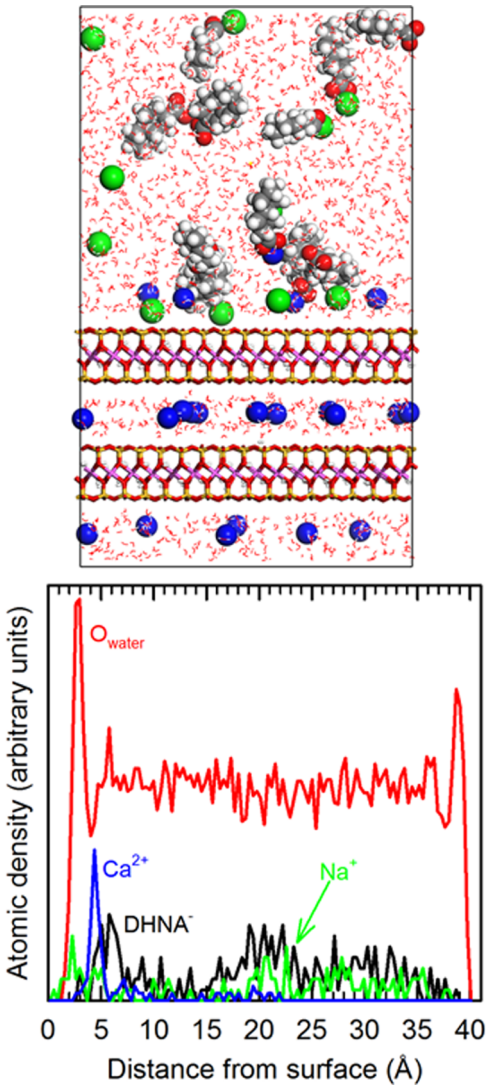

Figure 3. Example of an initial configuration used for the MD simulations (top) and the corresponding 1D atomic density profile from a 0.2 ns MD simulation at 1000 K (bottom). The model system contains two layers of hydrated Ca-montmorillonite and an aqueous pore with $DHNA^-$, Na^+, and Ca^{2+} (large spheres). Atoms are colored Si (yellow), Al (pink), Mg (dark purple), O (red), H (white), Ca (blue), Na (green), and C (gray). Density profiles are shown as a function of distance from the montmorillonite surface (siloxane oxygen atoms).

simulations, atoms other than hydrogen in the clay layers were held fixed to prevent the clay layers from drifting.

In order to verify that a production simulation time of 2.0 ns is sufficiently long to capture the organic adsorption phenomena, one kaolinite system with DHNA molecules was simulated for an additional 50 ns. A comparison of atomic density profiles at the end of the 50 ns simulation with the averaged profiles from 20 shorter (2 ns) simulations (data not shown) indicates that the aqueous structure that formed during the first 2 ns was only slightly modified after 50 ns. Over the longer simulation time, the organic molecules become well separated into an adsorbed layer and a desorbed layer at the vacuum interface. However, the ratio of adsorbed and desorbed DHNA molecules is unchanged between the short and long time scales. We note that the primary partitioning of solute molecules into adsorbed and desorbed phases occurs during the initial 0.5 ns of MD simulation, prior to data collection.

3. RESULTS AND DISCUSSION

3.1. DFT Geometry Optimizations. In contrast to the classical MD models, the periodic DFT calculations do not have any water molecules present in the simulation cell. Solvation effects are ignored due to the difficulty in obtaining fully minimized structures at 0 K with a large assembly of water molecules that would have an intractable number of possible configurations. Our results indicate that the hydroxylated kaolinite surface is relatively unique for a clay substrate by the nature of its hydrophilic surface. The extent of interaction of the organic compound with the kaolinite surface is dependent on the existence and nature of polar or ionized functional groups, and on the presence of a bridging cation such as Na^+ or Ca^{2+}. Additional insights were obtained by comparing these results with similar calculations using less hydrophilic clay substrates such as the basal siloxane surface of 2:1 clays like pyrophyllite and montmorillonite.

Calculation of binding energies for dry models (Table 3) aids in the identification of the most stable configurations and reconcile the preferred binding mechanisms. Binding energies are derived by taking the difference in potential energy between the associated (adsorbed) state and the isolated reactant state for each system. The column labeled "associated" includes binding energies derived for a stable complex that is adsorbed directly onto the substrate as a unit rather than from its isolated components. Using the Ca^{2+}–toluene complex on kaolinite as an example, the "isolated" binding energy was calculated using three reactant energies (Ca^{2+}, toluene, kaolinite), while the "associated" binding energy was calculated using two reactant energies (Ca^{2+}–toluene, kaolinite). The negative energy values represent the favorable gain in energy with the molecule in the adsorbed state compared to the isolated state away from the clay surface. Energy values represent the 0 K state of the molecule or surface. All but one of the molecular optimizations met the full convergence criteria; the montmorillonite–$DHNA^-$ simulation failed after 81 optimization steps but was within ten percent of the atom displacement criteria and had met all other convergence values.

In contrast to adsorption energies, the binding energies reported in Table 3 only represent the direct interaction of the clay substrate with the adsorbate. The adsorption energy accounts for the competition between the adsorbed site on the clay and the solvated state of the molecule in solution away from the surface. The use of DFT optimization precludes the incorporation of solvation as noted previously, but assuming hydration effects for the organic molecules are relatively small, the binding energies can be used to represent the overall adsorption process.

The calculated binding energies indicate the most favored clay interactions are associated with the adsorption of $DHNA^-$ and of the bare cations. The binding energies for Na^+ and Ca^{2+} are in agreement with the energies derived using a similar method for the analysis of cation adsorption on related clays.[51] Calculated binding energies for the organic interactions with clay minerals are enhanced by the coordinated adsorption of the organic molecule with Ca^{2+} and to a lesser extent Na^+ onto the surface. For example, adsorption of only toluene onto kaolinite is approximately -13 kcal·mol^{-1}, but in association with Na^+ or Ca^{2+} the binding energy increases to -112 and -376 kcal·mol^{-1}, respectively. Similarly, Na^+ and Ca^{2+}

DOI: 10.1021/acs.jpcc.7b06454
J. Phys. Chem. C 2017, 121, 22773–22786

Table 3. DFT Binding Energies (kcal·mol^{-1}) for Ions and Molecules Adsorbed to Clay Surfaces

surface	complex	isolated	associated
	Ca^{2+}−DHNA$^-$	−345.4	
	Ca^{2+}−toluene	−92.1	
	Na^+−DHNA$^-$	−164.5	
	Na^+−toluene	−36.1	
kaolinite	Ca^{2+}	−336.2	
	Na^+	−89.4	
	hexane	−11.2	
	cyclohexane	−10.7	
	toluene	−13.2	
	Ca^{2+}−toluene	−376.4	−284.3
	Na^+−toluene	−112.2	−76.0
	DHNA	+11.6	
	DHNA$^-$	−77.6	
	Ca^{2+}−DHNA$^-$	−472.2	−126.7
	Na^+−DHNA$^-$	−188.8	−24.2
pyrophyllite	Ca^{2+}	−350.1	
	Na^+	−101.5	
	hexane	−11.23	
	cyclohexane	−8.5	
	toluene	−12.2	
	Ca^{2+}−toluene	−393.6	−301.5
	Na^+−toluene	−126.7	−90.6
	DHNA	−16.3	
	DHNA$^-$	−36.9	
	Ca^{2+}−DHNA$^-$	−465.6	−120.2
	Na^+−DHNA$^-$	−160.9	+3.6
montmorillonite	Ca^{2+}	−371.0	
	Na^+	−122.0	
	hexane	−12.4	
	cyclohexane	−10.2	
	toluene	−12.4	
	Ca^{2+}−toluene	−409.5	−317.4
	Na^+−toluene	−147.8	−111.6
	DHNA	−17.1	
	DHNA$^-$	−27.6	
	Ca^{2+}−DHNA$^-$	−474.5	−129.0
	Na^+−DHNA$^-$	−172.0	−7.45

association with DHNA$^-$ results in significantly greater binding energies than the association energy without the presence of the clay: up to 15% for Na^+ and 35−38% for Ca^{2+}. Similar enhancements of organic binding are observed in the DFT results for pyrophyllite and montmorillonite in the presence of cations. However, these energies assume that the reactants are isolated from each other and not associated in solution.

The neutral adsorbates exhibit relatively small binding energies (on the order of −10 to −15 kcal·mol^{-1}). Within the constraints of the nonlocal GGA and the DNP basis set, the results clearly quantify the limited binding (slightly negative or slightly positive binding energy) for neutral organic molecules across all clay surfaces. Interestingly, the representative resin molecule DHNA interacts with the siloxane clay surfaces (i.e., montmorillonite and pyrophyllite) through short-range interactions between the cyclic aliphatic hydrocarbon and siloxane hexagonal rings. The hydroxylated kaolinite surface has no such ring structure available, and as a result, the DHNA binding energy is positive. Enhanced ring−ring interactions were also used to explain more favorable adsorption of the polycyclic organic dye methylene blue on the siloxane surface of kaolinite rather than the hydroxylated surface.[52]

Adsorption of Na^+− and Ca^{2+}−organic complexes onto the charged montmorillonite surface is slightly enhanced relative to the uncharged surface of pyrophyllite. The charged substitutional sites associated with the octahedral sheet of montmorillonite (Mg^{2+} for Al^{3+}) affect the binding and local structure of the adsorbate. Interestingly, adsorption of Na^+− or Ca^{2+}−toluene complexes is much less favorable on the hydroxylated kaolinite surface, presumably due to the disruption of ring−ring interactions in the presence of a cation. However, the hydrophilic kaolinite surfaces enhance the adsorption of Na^+−DHNA$^-$ relative to the siloxane surfaces, and the Ca^{2+}−DHNA$^-$ complexes have a similar binding energy on either the kaolinite or montmorillonite surfaces. Finally, we note that the Ca^{2+}−organic complexes have much lower binding energies on all surfaces compared to the Na^+ analogues, even considering associated rather than isolated binding energies (Table 3). This result suggests that the presence of the bridging ion, particularly Ca^{2+}, significantly influences the binding of organics onto clay mineral surfaces.

Examples of ion bridging mechanisms are evident in DFT-optimized structures of DHNA and Ca^{2+}−DHNA$^-$ adsorbed on kaolinite and montmorillonite structures (Figure 4). The neutral DHNA molecule is similarly adsorbed to either surface through mostly the carboxyl group for both surfaces and additionally by hydrophobic interactions with the montmorillonite surface. However, with a bridging Ca^{2+}, which is strongly coordinated to the carboxylate group, DHNA$^-$ is more closely bound to the identical surfaces than as a neutral molecule. The Ca^{2+}−DNHA$^-$ complex binds to the hydroxylated surface of kaolinite and to the charged montmorillonite surface. The strong electrostatic interactions between the Ca^{2+} and the charged octahedral site (substitution of Mg^{2+} for Al^{3+}) of montmorillonite control the local binding environment (Figure 4d).

DFT calculations were also used to validate the hybrid force field approach used in the classical MD simulations. Such validation is needed to confirm the accuracy of the force fields in simulating more complex models like the organic−clay systems of the present study. As examples, Figure 5 presents optimized structures of DHNA molecules adsorbed on the kaolinite and pyrophyllite surfaces. While the clay structures and the disposition of their hydroxyl groups are similar, the relative agreement in adsorbate structure depends on the degree of hydrophilic interaction between adsorbate and substrate. DHNA−pyrophyllite complexes are dominated by hydrophobic interactions, resulting in close structural agreement between the two methods. A noticeable difference in adsorbate structure is seen for DHNA adsorbed on the kaolinite surface. In this case, the molecule is tilted to facilitate hydrogen bonding between the organic carboxylic acid group and surface hydroxyls. The force field-optimized structure indicates a stronger adsorption interaction, while the DFT-optimized structure shows weaker adsorbate−substrate hydrogen bonding. One caution in this comparison of the two simulation methods is the deficiencies in evaluating dispersion interactions in our DFT approach, which would be a concern primarily for those simulations involving neutral clay and organic molecular interactions.[53]

Calculated binding energies are compared in Table 4, indicating overall general agreement of the methods and a validation of our force field approach. In particular, the classical

DOI: 10.1021/acs.jpcc.7b06454
J. Phys. Chem. C 2017, 121, 22773−22786

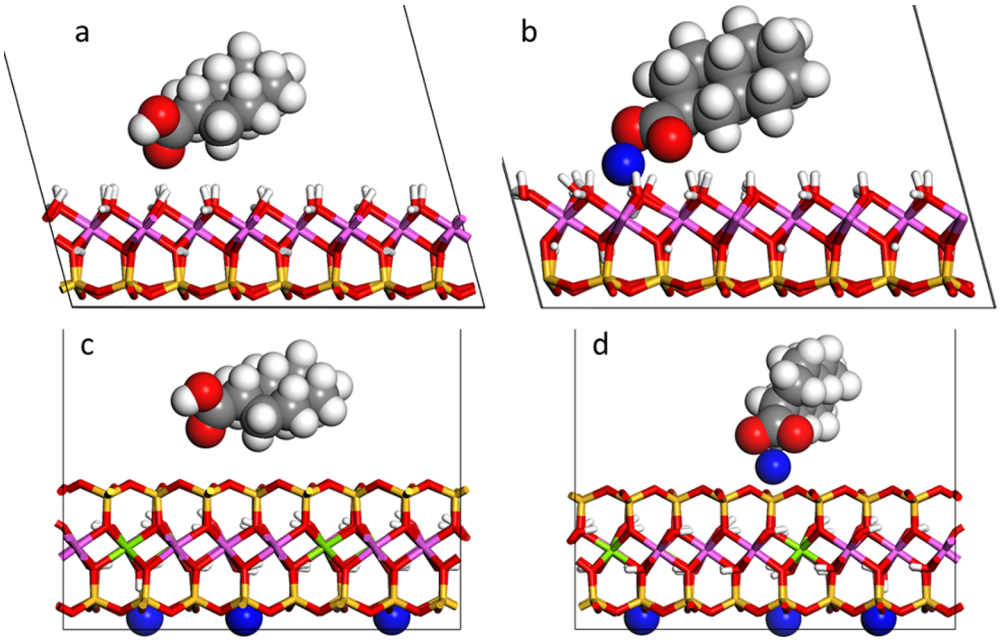

Figure 4. DFT-optimized structures of $DHNA^-$ surface complexes: (a) DHNA on kaolinite, (b) Ca^{2+}–$DHNA^-$ on kaolinite, (c) DHNA on montmorillonite, and (d) Ca^{2+}–$DHNA^-$ on montmorillonite. Top-down views are provided in the Supporting Information.

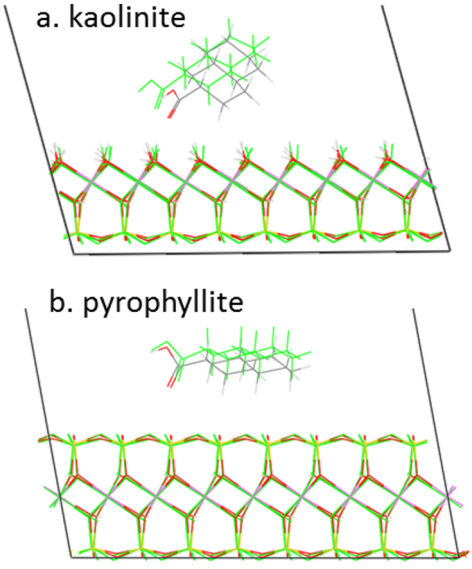

Figure 5. Comparison of DFT (green) and classical (light gray, gray, and red) optimized structures for the adsorption of DHNA onto (a) kaolinite and (b) pyrophyllite.

Table 4. Comparison of DFT and Classical Binding Energies in the Gas Phase and on Clay Surfaces

		binding energy (kcal·mol^{-1})	
surface	complex	DFT	classical
gas phase	Ca^{2+}–$DHNA^-$	−345.4	−365.7
	Na^+–$DHNA^-$	−164.5	−150.1
	Na^+–toluene	−36.1	−13.1
pyrophyllite	Na^+	−101.5	−69.1
	Ca^{2+}	−350.1	−238.2
	DHNA	−16.3	−9.7
	Ca^{2+}–$DHNA^-$	−465.6	−402.8
kaolinite	Na^+	−89.4	−74.2
	DHNA	11.6	−12.4
	Na^+–$DHNA^-$	−188.8	−200.8
	toluene	−13.2	−13.4
	Na^+–toluene	−126.7	−91.0
	hexane	−11.2	−8.6
	cyclohexane	−10.7	−7.6

binding energies correctly predict the trend of low binding energies when hydrophobic interactions dominate and high binding energies when electrostatic interactions dominate. Therefore, for clarity, Table 4 only includes binding energies of organic species on the kaolinite surface and DHNA on the pryophyllite surface. Comparing the binding energies for DHNA complexes on kaolinite and pyrophyllite with the optimized structures (Figure 5), the force field-optimized DHNA–pyrophyllite structure is nearly overlaid on the DFT structure, and the force field binding energy is only 6.6 kcal·mol^{-1} lower. Hydrogen bonding between DHNA molecules and the kaolinite surface results in a slightly attractive binding energy for the force field example, but the reduced degree of hydrogen-bonding in the DFT-optimized structure results in a slightly repulsive binding energy.

Table 4 also includes a comparison of cation binding energies on the pyrophyllite surface, which shows that Clayff underpredicts DFT by approximately 30%. Examination of cation–oxygen distances from optimized structures reveals that Clayff predicts larger cation–oxygen distances on pyrophyllite (Ca–O distances: resulting in weaker cation binding to the surface). Relevant distances for Ca–O are 2.53 Å (Clayff) and 2.36 Å (DFT), and for Na–O, they are 2.53 Å (Clayff) and 2.44 Å (DFT).

3.2. Classical MD Simulations. The adsorption of aqueous species on substrate surfaces is determined by monitoring atomic positions throughout the production portion of an MD simulation, resulting in one-dimensional atomic density profiles. Solute and water peaks at the mineral–solution interface represent adsorption layers, and these peaks can be integrated to determine the relative proportion of each species present in

DOI: 10.1021/acs.jpcc.7b06454
J. Phys. Chem. C 2017, 121, 22773–22786

those layers. For organic solutes, atomic density profiles were calculated from carbon atoms as follows: aliphatic carbon atoms in toluene and the hexanes, and carboxylic C atoms for DHNA and $DHNA^-$ since this atom type is present in both the protonated and deprotonated forms. Each profile represents an average of the 20 replicate simulations, each averaged over the final 2.0 ns of the simulation. As seen in the atomic density profiles to follow, some of the surface complexes are essentially static over the time scale of our simulations (zero density in regions far from the surface). Since residence times cannot be calculated in those situations, we have not attempted to calculate them for any of the simulations. The percent adsorbed values calculated from the atomic density profiles are an indicator of the binding affinity for each species, rather than a time-dependent property such as residence time.

Sample atomic density profiles from simulations at 300 K are shown in Figure 6 for the adsorption of a hydrophobic organic molecule (hexane) on all three clay mineral surfaces. Almost no adsorption of the hydrophobic organics is seen at the kaolinite surface, but instead, the hexane molecules form a hydrophobic phase at the vacuum interface (Figure 6a, peaks between 28−34 Å). Hydrophobic interactions result in strong adsorption of hexane molecules on the pyrophyllite surface (Figure 6b, peaks at 3−4 Å), but a hydrophobic phase still forms at the vacuum interface. The montmorillonite results are intermediate between kaolinite and pyrophyllite. Although the siloxane surface of montmorillonite is considered to be hydrophilic due to the presence of adsorbed counterions, neutral organics are able to adsorb at hydrophobic regions where no charge sites or adsorbed ions are present. Increasing the salinity with Ca^{2+} and Cl^- in the aqueous region has little effect on adsorption of the hydrophobic organics. Although the gas-phase binding of these molecules is enhanced in the presence of cations (Table 4), there is little or no association of these molecules with aqueous ions.

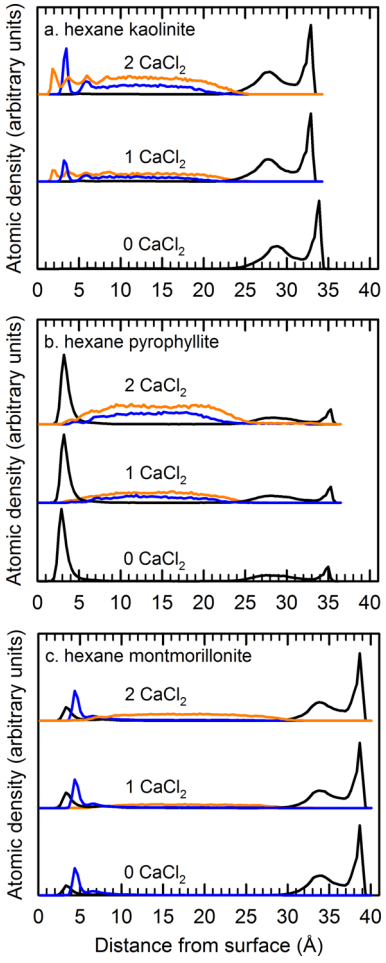

Figure 6. Atomic density profiles showing hexane (carbon atoms, black lines) and aqueous ions (Ca^{2+}, blue lines; Cl^-, orange lines) as a function of distance from (a) kaolinite (hydroxyl oxygen atoms), (b) pyrophyllite, and (c) montmorillonite surfaces from MD simulations at 300 K. Salinity was varied by adding increasing amounts of Ca^{2+} and Cl^- to the aqueous region, as indicated. Density profiles were averaged over 20 separate production simulations of 2 ns each.

Density profiles from the resin simulations (Figure 7) indicate that resin adsorption depends on several factors, including resin protonation, surface charge, and surface hydrophobicity. Profiles for the neutral DHNA molecule are similar to those observed for hexane (Figure 6), with some slight variations in organic carbon peaks due to differences in molecular geometry and hydrophilicity. Despite the presence of a hydrophilic carboxylic acid group, DHNA molecules only interact with hydrophobic surfaces (including to some extent montmorillonite) with almost no adsorption on the kaolinite surface. Changes in salinity do not affect DHNA adsorption; no evidence of cation coordination is seen in the density profiles. In contrast, the coincidence of $DHNA^-$ peaks with cation peaks in each model system indicates that these organic anions readily coordinate to cations in both the adsorbed and desorbed phases. The presence of two resin density peaks near the siloxane surfaces of pyrophyllite and montmorillonite indicate two possible orientations of adsorbed molecules for both the neutral and anion forms. Details of these surface complexes will be discussed below with the aid of MD snapshot images.

The most noticeable difference in adsorption behavior between the neutral and anion forms of the resin are seen at the kaolinite surface (Figure 7a,b). While DHNA molecules do not adsorb to the kaolinite surface, Na^+−$DHNA^-$ pairs are strongly adsorbed at all $CaCl_2$ concentrations. Salinity effects are seen as Ca^{2+} is added to the aqueous region, but only at the highest ionic strength (two $CaCl_2$) are calcium ions adsorbed at the surface. The broad peaks near the vacuum interface (Figure 7b, 25 Å) and their associated cation peaks indicate that desorbed $DHNA^-$ is coordinated by both Na^+ and Ca^{2+}. At intermediate $CaCl_2$ concentration, $DHNA^-$ adsorption is slightly reduced due to the formation of Ca^{2+}−$DHNA^-$ complexes at the vacuum interface. As more $CaCl_2$ is added to the aqueous region, Ca^{2+} is adsorbed at the surface along with additional $DHNA^-$. Hydrophobic interactions control the adsorption of $DHNA^-$ on the pyrophyllite surface, as indicated by a broad layer of adsorbed $DHNA^-$ (Figure 7d). Cation density peaks are shifted away from the surface, indicating that cation−$DHNA^-$ complexes are oriented with the hydrophilic end pointing toward the aqueous region. A subtle difference in adsorption behavior between DHNA and $DHNA^-$ occurs at the montmorillonite surface (Figures 7e,f). For DHNA, the organic peak is closer to the surface than adsorbed cations, indicating that DHNA molecules interact directly with the surface. However, cation peaks are closer to the surface than $DHNA^-$, indicative of a cation bridging adsorption mechanism.

Integrated areas under each adsorption peak in the solute density profiles were used to calculate the percent adsorption. Both strong and weak adsorption were considered in our

DOI: 10.1021/acs.jpcc.7b06454
J. Phys. Chem. C 2017, 121, 22773−22786

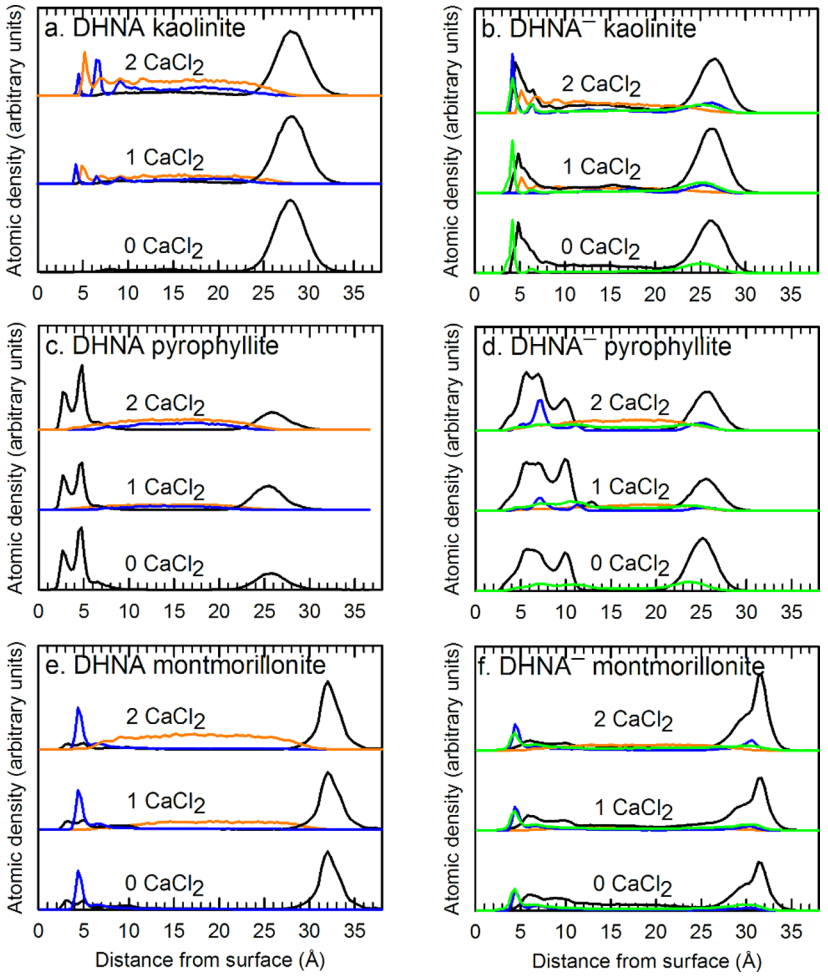

Figure 7. Atomic density profiles from MD simulations at 300 K showing DHNA (a,c,e) and $DHNA^-$ (b,d,f; carboxylate carbon atoms; black lines) and aqueous ions (Ca^{2+}, blue lines; Na^+, green lines; Cl^-, orange lines) as a function of distance from surface oxygen atoms of kaolinite, pyrophyllite, and montmorillonite. Density profiles were averaged over 20 separate production simulations of 2 ns each.

analysis of atomic density profiles. The minimum in the first density peak near the surface defines the boundary between "strongly adsorbed" and "weakly adsorbed" molecules. The upper limit for weakly adsorbed species was also identified by a minimum in the density profile, approximately 10 Å from the surface. For most model systems simulated, adsorbed and desorbed organic layers are well partitioned, as seen in the density profiles (Figures 6 and 7). Uncertainties in the reported percent adsorption values are approximately 10% (e.g., 50% implies a range of 40−60%). This uncertainty reflects the number of replicate simulations for each system (20) and the effect of initial configuration of the aqueous region.

Adsorption percentages for the saturates and the aromatic (toluene) are shown in Figure 8. These hydrophobic molecules are strongly adsorbed to the neutral siloxane surface of pyrophyllite and to a much lesser extent to the charged siloxane surface of montmorillonite. While cyclohexane and toluene might be expected to form stronger interactions with the siloxane surfaces through ring−ring interactions, cyclohexane adsorption on pyrophyllite is lower than the linear hexane or aromatic toluene molecules. However, the adsorption of toluene on montmorillonite is significantly greater than the saturate molecules. Toluene molecules interact directly with the montmorillonite surface but not with adsorbed Ca^{2+}, as observed in gas-phase DFT calculations.

The hydroxylated kaolinite surface provides no interaction sites for these molecules, resulting in almost no adsorption. As expected, changes in salinity have little or no effect on the adsorption of saturates or aromatics since these molecules interact with mineral surfaces primarily through hydrophobic interactions. Temperature effects are only apparent at the montmorillonite surface, where increased kinetic energy at high temperature results in reduced adsorption. In the presence of an aqueous solution, these molecules tend to form a hydrophobic (oil-wet) phase, either at a hydrophobic surface such as pyrophyllite or at the vacuum interface (Figure 6).

Both resin species are able to form strong hydrophilic interactions with mineral surfaces and water molecules, but adsorption trends for these species (Figure 9) are surprisingly similar to those for the hydrophobic organics. The strongest adsorption occurs at the pyrophyllite surface, with significantly reduced adsorption at the montmorillonite surface. Atomic density profiles (Figure 7) along with MD snapshots and radial distribution results (shown below) confirm that most $DHNA^-$ form Na^+ and Ca^{2+} complexes in solution and at the mineral interfaces, resulting in neutral or positively charged Na^+−$DHNA^-$ and Ca^{2+}−$DHNA^-$ species. The strongest salinity effects are seen at the pyrophyllite surface but with opposite behavior for DHNA (adsorption decreases with increased salinity) compared with $DHNA^-$ (adsorption increases with

DOI: 10.1021/acs.jpcc.7b06454
J. Phys. Chem. C 2017, 121, 22773−22786

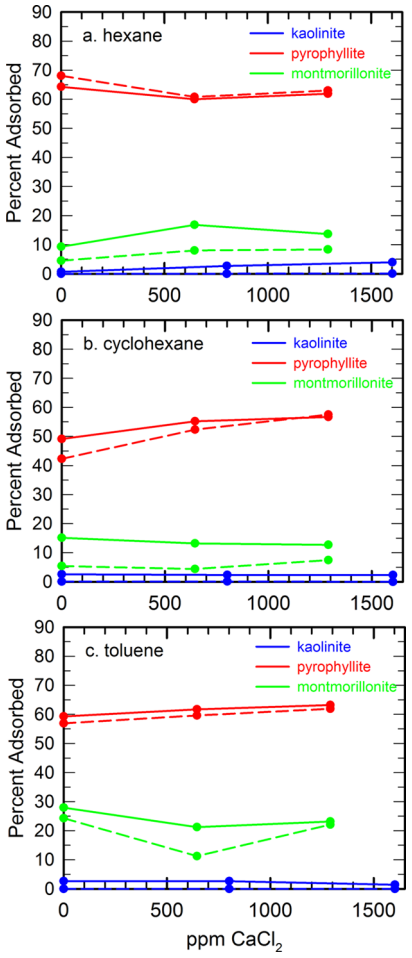

Figure 8. Comparison of (a,b) saturates (hexanes) and (c) aromatic (toluene) adsorption on kaolinite, pyrophyllite, and montmorillonite surfaces from MD simulations at 300 K (solid lines) and 366 K (dashed lines), and as a function of $CaCl_2$ concentration.

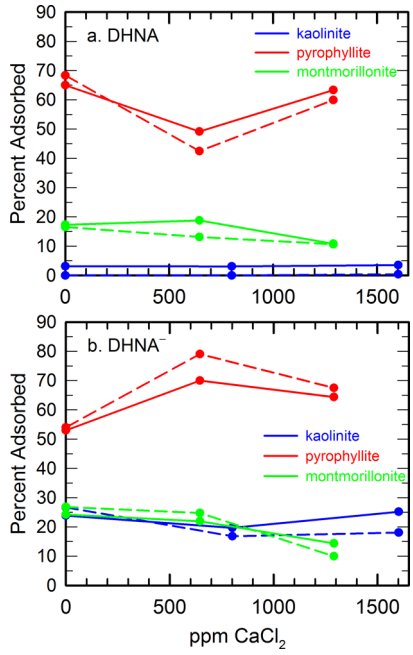

Figure 9. Comparison of (a) neutral resin (DHNA) and (b) anionic resin ($DHNA^-$) adsorption on kaolinite, pyrophyllite, and montmorillonite surfaces from MD simulations at 300 K (solid lines) and 366 K (dashed lines), and as a function of aqueous $CaCl_2$ concentration. The percent adsorbed values represent both strongly and weakly adsorbed molecules.

increased salinity). Although DHNA molecules do not form complexes with Ca^{2+}, the presence of these ions results in significant desorption of DHNA from the surface. Because montmorillonite bears a permanent structural charge, the aqueous region contains a high concentration of Ca^{2+} (4800 ppm). As a result of the strong electrostatic interactions between hydrated calcium ions and the montmorillonite surface, increasing the ionic strength has little effect on the adsorption tendencies of DHNA or $DHNA^-$.

Other than the difference in salinity effects at the pyrophyllite surface, the other quantifiable difference in adsorption behavior between resin forms occurs at the kaolinite surface, where the anion shows moderate adsorption (20−30%) compared to the near-zero adsorption of the neutral molecule. Despite the presence of a carboxylic acid group, neutral DHNA molecules interact only weakly with the kaolinite surface, as noted previously from the density profiles (Figure 7) and the low DFT binding energy for DHNA on kaolinite (Table 3). Instead, they form an organic phase at the water−vacuum interface. In contrast, $DHNA^-$ adsorbs to the kaolinite surface at both low temperature and high temperature, and the density profiles confirm that most $DHNA^-$adsorb to kaolinite as neutral Na^+−$DHNA^-$ complexes.

In most cases, resin adsorption decreases as temperature increases since these species have more thermal energy to overcome the activation energy required to desorb. Interestingly, $DHNA^-$ adsorption increases at higher temperature near the pyrophyllite surface when Ca^{2+} is present and near the montmorillonite surface at intermediate $CaCl_2$ concentration. At high temperature and in the presence of strongly complexing calcium ions, Na^+−$DHNA^-$ and Ca^{2+}−$DHNA^-$ complexes are mobile in the aqueous phase, so opportunities for adsorption to siloxane surfaces (pyrophyllite or montmorillonite) are increased.

Assuming a pK_a of less than 5 for the DHNA molecule,[54] we expect the anionic form to be dominant in most oil reservoirs. At all temperatures and ionic strengths considered in the MD simulations, significantly more $DHNA^-$ is adsorbed on the hydrophobic pyrophyllite surface than either of the hydrophilic kaolinite or Ca-montmorillonite surfaces. The atomic density profiles and trajectory snapshots exhibit significant ion pairing between $DHNA^-$ ions and aqueous cations in both adsorbed and desorbed states. Consequently, neutral Na^+−$DHNA^-$ or positively charged Ca^{2+}−$DHNA^-$ complexes are most strongly attracted to the neutral pyrophyllite surface. Adsorption of $DHNA^-$ is reduced at the hydrophilic surfaces (kaolinite and montmorillonite), presumably due to the hydrophobic nature of the resin molecule or anion.

MD snapshots of the resin species adsorbed on the pyrophyllite surface (Figure 10) show that neutral DHNA molecules tend to adsorb on the pyrophyllite surface such that the cyclohexane rings of DHNA are parallel to the siloxane rings of pyrophyllite. This arrangement maximizes hydrophobic interactions. The structure of adsorbed $DHNA^-$ is noticeably different, with the negatively charged carboxyl groups (and coordinated sodium ions) located as far from the surface as possible while still maximizing hydrophobic interactions with the surface. As a result, the relative distance of the carboxylate C atoms to the pyrophyllite surface is greater for $DHNA^-$ than

DOI: 10.1021/acs.jpcc.7b06454
J. Phys. Chem. C 2017, 121, 22773−22786

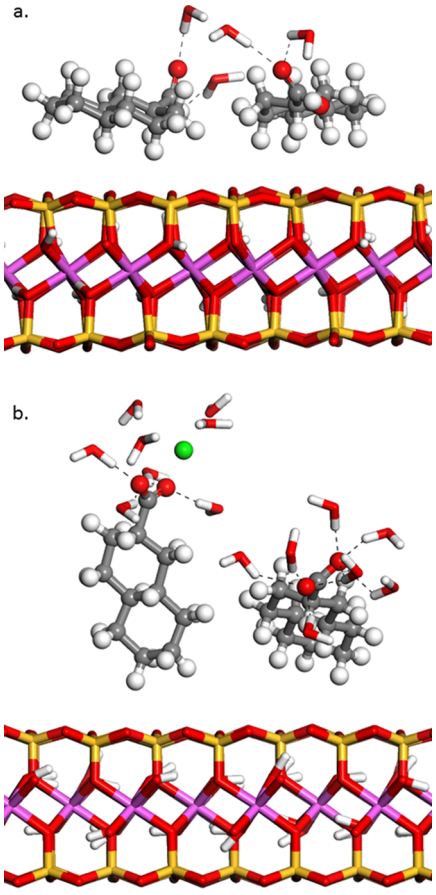

Figure 10. Snapshots from MD simulations at 300 K with no added $CaCl_2$ (0 ppm of $CaCl_2$) showing (a) DHNA and (b) $DHNA^-$ adsorbed on the pyrophyllite surface. Water molecules coordinating to carboxylate groups and sodium ions are also shown, with hydrogen bonds (dashed black lines). Atoms are colored as in Figure 1. Top-down views are provided in the Supporting Information.

DHNA. The corresponding density profiles (Figures 7c,d) show that the $DHNA^-$ peaks are shifted approximately 5 Å farther from the surface than DHNA. We conclude that both DHNA and $DHNA^-$ interact strongly with the pyrophyllite basal surface, but through different mechanisms.

Almost no DHNA adsorption is observed on the kaolinite surface (Figure 7a), but $DHNA^-$ adsorption is characterized by cation coordination and hydrogen bonds with surface hydroxyl groups (Figure 11). The cation complexes are consistent with the gas-phase DFT results (Figure 4b), and in aqueous solution, the adsorption of neutral complexes such as Na^+–$DHNA^-$ and Ca^{2+}–$(DHNA^-)_2$ is preferred. Note that $DHNA^-$ adsorbs directly to the surface via hydrogen bonding rather than through an ion bridging mechanism. The first coordination shells of adsorbed Na^+ and Ca^{2+} consists of oxygen atoms from $DHNA^-$, water, and surface hydroxyl groups. The adsorption of an organic anion such as $DHNA^-$ should make the kaolinite surface more oil-wet, and indeed, this has been confirmed in a recent experiment where the wettability of kaolinite was modified from water-wet to oil-wet by adding a similar organic anion (sodium naphthenate) to an oil–water emulsion containing kaolinite.[55]

As in the pyrophyllite systems, similar amounts of DHNA and $DHNA^-$ are adsorbed on the montmorillonite surface, but snapshots of the surface complexes (Figure 12) reveal very

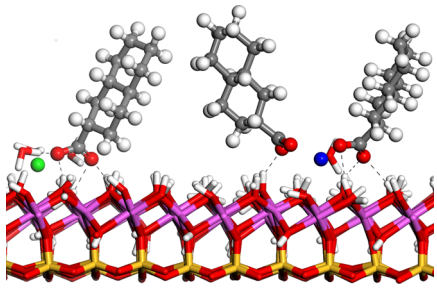

Figure 11. Snapshot from MD simulations at 300 K with no added $CaCl_2$ (0 ppm of $CaCl_2$) showing Na^+–$DHNA^-$ and Ca^{2+}–$(DHNA^-)_2$ complexes adsorbed onto the hydroxylated kaolinite surface. Water molecules coordinating to carboxylate groups and cations are also shown, with hydrogen bonds (dashed black lines). Atoms are colored as in Figure 1.

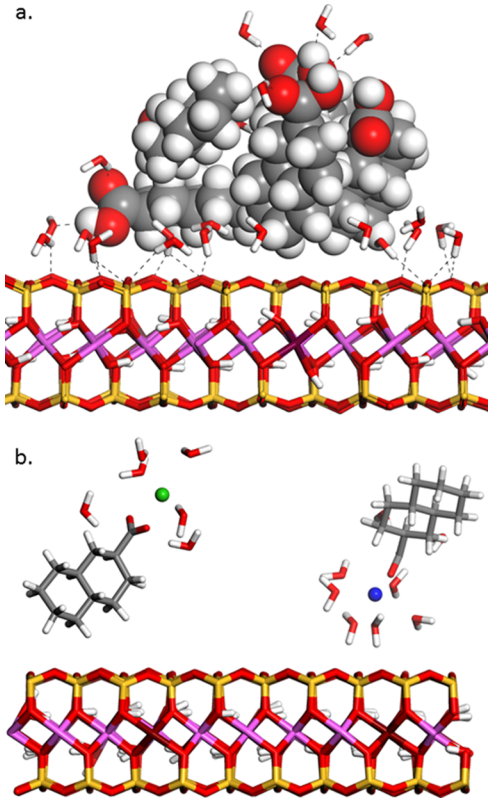

Figure 12. Snapshots from MD simulations of montmorillonite interfaces at 300 K showing (a) adsorbed DHNA molecules and (b) adsorbed Na^+–$DHNA^-$ and Ca^{2+}–$DHNA^-$ complexes. Nearest neighbor water molecules are also shown along with select hydrogen bonds (dashed black lines). Atoms are colored as in Figure 1.

different adsorption mechanisms. DHNA molecules adsorb directly to the montmorillonite surface through hydrophobic interactions (i.e., no intervening water molecules or cations). Two types of DHNA–montmorillonite surface complexes are shown in Figure 12a. In one case, DHNA molecules are oriented parallel to the surface to enhance ring–surface interactions, as seen on the pyrophyllite surface (Figure 10a). The other type of surface complex is similar to the Na^+–$DHNA^-$ complexes that form on the pyrophyllite surface, with the carboxylic acid group far from the surface to facilitate hydrophobic interactions through CH_2 groups. Some $DHNA^-$ ions adsorb onto montmorillonite through cation bridging, but

DOI: 10.1021/acs.jpcc.7b06454
J. Phys. Chem. C 2017, 121, 22773–22786

small cation density peaks approximately 7 Å from the surface (Figure 7f) indicate that the hydrophobic end of $DHNA^-$ can interact directly with the surface. Both types of $DHNA^-$ surface complexes are seen in Figure 12b.

The relative abundance of cation−$DHNA^-$ complexes provides additional insight into the $DHNA^-$ adsorption trends discussed previously. Radial distribution functions of oxygen−cation pairs were used to determine the fraction of $DHNA^-$ that are coordinated to cations (Figure 13a). For the kaolinite

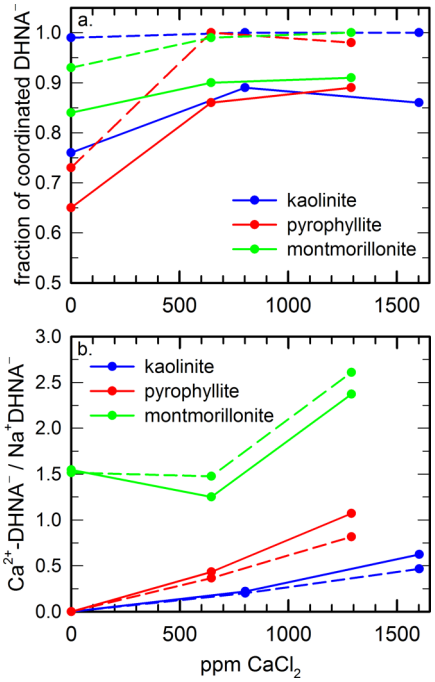

Figure 13. $DHNA^-$ coordination by aqueous cations obtained from MD radial distribution functions at 300 K (solid lines) and 366 K (dashed lines). (a) Fraction of $DHNA^-$ coordinated by an aqueous cation, including Na^+ and Ca^{2+}. (b) Ratio of $DHNA^-$ coordinated by Ca^{2+} and Na^+.

and pyrophyllite systems, higher salinity (added Ca^{2+}) results in an increase in total $DHNA^-$ coordination. The fraction of coordinated $DHNA^-$ is higher in the montmorillonite system compared to the neutral surfaces because the aqueous region near the montmorillonite surface always contains six charge-balancing Ca^{2+} ions. Pyrophyllite systems with $CaCl_2$ of 645 and 1290 ppm contain one and two Ca^{2+} ions, respectively, while the corresponding montmorillonite systems contain seven and eight Ca^{2+}. Cation−$DHNA^-$ complexes are also more likely to form at higher temperature. The increased kinetic motion at higher temperature increases the likelihood of $DHNA^-$ interactions with cations, resulting in strong complexes with gas-phase association energies of −164.5 and −345.4 kcal·mol^{-1} for Na^+ and Ca^{2+}, respectively (Table 4).

Compared to the neutral surfaces, the presence of additional Ca^{2+} near the montmorillonite surface results in a large ratio of Ca-coordinated $DHNA^-$ compared to Na-coordinated $DHNA^-$ (Figure 13b). The aqueous regions near the neutral surfaces contain far more Na^+ than Ca^{2+}: 12 and 14 Na^+ for kaolinite and pyrophyllite, respectively, compared with one and two Ca^{2+} at intermediate and high ppm values. Despite the small fraction of Ca^{2+} in these aqueous regions, a significant fraction of $DHNA^-$ is coordinated by Ca^{2+} through calcium-bridged dimers in both the adsorbed and desorbed states (cf. Figure 11).

Trends in cation coordination can be correlated with trends in $DHNA^-$ adsorption, using, for example, results for the pyrophyllite system at 300 K. With no $CaCl_2$, 65% of $DHNA^-$ are coordinated to Na^+ and 65% of $DHNA^-$ are adsorbed. With one added $CaCl_2$ (645 ppm), more than twice as many $DHNA^-$ are coordinated by Na^+ than Ca^{2+} (Ca^{2+}/Na^+ ratio of 0.4 in Figure 13b), and the percent adsorption decreases slightly to 60%. The addition of a second $CaCl_2$ (1290 ppm) increases the ratio of $DHNA^-$ coordinated to Ca^{2+} vs Na^+ to near unity, but the percent $DHNA^-$ adsorption is unaffected. The formation of positively charged Ca^{2+}−$DHNA^-$ complexes correlates with a slight reduction in adsorption on a neutral surface such as pyrophyllite.

4. CONCLUSIONS

Atomistic simulations provide a more realistic model of the interfacial behavior of organic−clay mineral systems than simple conceptual models used previously to reconcile the competition of crude oil molecules with aqueous phases for the mineral surface. The ability of a mineral surface to wet with oil or with water ultimately determines the extent to which residual oil can be recovered from a reservoir. In this work, simulations were performed at the quantum and classical levels of theory to investigate the adsorption of crude oil components on clay mineral surfaces. Particular focus was placed on a representative resin molecule (DHNA) and its anion form ($DHNA^-$) expected to be prevalent in aqueous solutions in oil reservoirs. The significant role of aqueous cations and their ability to strongly bind to clay surfaces is confirmed through molecular simulation at both levels of theory. Although montmorillonite surfaces bear a permanent (negative) structural charge, the adsorption of aqueous cations such as Na^+ and Ca^{2+} renders them essentially charge-neutral when adsorption onto the external basal surfaces is considered. However, layer charge does affect the extent of cation and organic adsorption, especially for 2:1 smectite clays based on comparisons between neutral pyrophyllite and charged montmorillonite systems.

Results from DFT simulations indicate that the binding energy of gaseous Na^+ or Ca^{2+} is largest for montmorillonite where octahedral Mg^{2+} enhances binding at the hexagonal siloxane ring. Cation bridging enhances organic adsorption onto all clay surfaces, especially when there is a strong association of the cation to the $DHNA^-$ carboxylate group or to the aromatic π electrons of toluene. The cation enhancement effect is particularly strong for Ca^{2+} compared to Na^+, based on the energy preference of Ca^{2+} for these surfaces (−336 to −371 kcal·mol^{-1}).

Because of the large computational cost of modeling the dynamics of explicit water molecules in DFT simulations, the quantum results of this study are limited. As a result, solvation effects on the structure and energetics of adsorption complexes are not considered. Fortunately, cost-effective classical models provide this flexibility and have been used in this study to examine solvation effects. The empirical force field used in the classical MD simulations (Clayff) has been validated using DFT methods for accuracy in determining structure and binding energy for selected adsorption models.

Classical MD results were used to compare adsorption trends as a function of temperature and ionic strength, in the form of increasing $CaCl_2$ concentration in the aqueous phase. The degree of adsorption for each surface−adsorbate system

DOI: 10.1021/acs.jpcc.7b06454
J. Phys. Chem. C 2017, 121, 22773−22786

correlates with the dominant intermolecular interaction favored by each species. Adsorption of all classes of organic molecules considered in this study is favored on the hydrophobic pyrophyllite surface. Although the representative resin molecule (DHNA) contains a carboxylic acid group that should favor hydrophilic interactions, the hydrophobic component of DHNA or its carboxylate anion ($DHNA^-$) strongly associates with hydrophobic surfaces. Hydrophobic interactions also result in moderate adsorption of all species on the negatively charged montmorillonite surface, which contains the same basal siloxane surface as pyrophyllite.

Only the anionic form of the resin ($DHNA^-$) shows significant adsorption on the hydroxylated kaolinite surface, forming surface complexes via cation bridging with either Na^+ or Ca^{2+}. Both DFT and MD results indicate that the preferred binding of $DHNA^-$ onto all surfaces considered in this study occurs via ion pairing with aqueous cations, although the carboxylate groups interact directly with surface hydroxyl groups of kaolinite. Ion pairing between $DHNA^-$ and aqueous cations occurs in the adsorbed and desorbed (hydrophobic) phases. In terms of salinity effects, only slight differences in organic adsorption and ion pairing were observed with added Ca^{2+}, but the $DHNA^-$ model systems already contain a high concentration of charge-balancing Na^+. As noted recently,[5] an electrical double layer forms at the montmorillonite surface, resulting in very few desorbed Ca^{2+} available for ion pairing in the desorbed hydrophobic phase.

Temperature effects on DHNA/$DHNA^-$ adsorption are not significant within the level of uncertainty of the simulations. The adsorption energies are sufficiently strong that an increase in temperature from 300 to 366 K results in little or no change in adsorption equilibrium. However, a slight decrease in adsorption in a few instances (saturates and aromatics on montmorillonite, $DHNA^-$ on kaolinite) is observed at the higher temperature, indicating weakly bound complexes.

The edges of clay minerals are almost certainly exposed in oil reservoir systems, especially in the sandstone reservoirs that contain kaolinite, which are currently produced in many basins of the world, and represent a pH-dependent site for the adsorption of hydrophilic organics. Typical montmorillonite and illite phases are dominated by basal surface areas, whereas kaolinite may have an extensive edge-site surface area that controls the adsorption of many of the organic molecules.

■ ASSOCIATED CONTENT

Supporting Information

The Supporting Information is available free of charge on the ACS Publications website at DOI: 10.1021/acs.jpcc.7b06454.

Select interatomic distances from optimized structures, top-down view of surface complexes, and LAMMPS input files containing force field parameters for each organic species (PDF)

■ AUTHOR INFORMATION

Corresponding Author

*E-mail: jagreat@sandia.gov.

ORCID

J. A. Greathouse: 0000-0002-4247-3362

R. T. Cygan: 0000-0003-1262-6177

Notes

The authors declare no competing financial interest.

■ ACKNOWLEDGMENTS

Sandia National Laboratories is a multimission laboratory managed and operated by National Technology and Engineering Solutions of Sandia, LLC., a wholly owned subsidiary of Honeywell International, Inc., for the U.S. Department of Energy's National Nuclear Security Administration under contract DE-NA0003525. This work was funded by BP America, and BP management is thanked for permission to publish this work.

■ REFERENCES

(1) Tang, G. Q.; Morrow, N. R. Influence of Brine Composition and Fines Migration on Crude Oil/Brine/Rock Interactions and Oil Recovery. *J. Pet. Sci. Eng.* **1999**, *24*, 99−111.

(2) Jerauld, G. R.; Lin, C. Y.; Webb, K. J.; Seccombe, J. C. Modeling Low-Salinity Waterflooding. *SPE Reservoir Eval. Eng.* **2008**, *11*, 1000−1012.

(3) Lager, A.; Webb, K. J.; Black, C. J. J.; Singleton, M.; Sorbie, K. S. Low Salinity Oil Recovery - an Experimental Investigation. *Petrophysics* **2008**, *49*, 28−35.

(4) Sposito, G. *The Chemistry of Soils*; Oxford University Press: New York, 1989.

(5) Underwood, T.; Erastova, V.; Cubillas, P.; Greenwell, H. C. Molecular Dynamic Simulations of Montmorillonite−Organic Interactions under Varying Salinity: An Insight into Enhanced Oil Recovery. *J. Phys. Chem. C* **2015**, *119*, 7282−7294.

(6) Sanchez, V. M.; Miranda, C. R. Modeling Acid Oil Component Interactions with Carbonate Reservoirs: A First-Principles View on Low Salinity Recovery Mechanisms. *J. Phys. Chem. C* **2014**, *118*, 19180−19187.

(7) de Lara, L. S.; Michelon, M. F.; Miranda, C. R. Molecular Dynamics Studies of Fluid/Oil Interfaces for Improved Oil Recovery Processes. *J. Phys. Chem. B* **2012**, *116*, 14667−14676.

(8) Zhong, J.; Wang, P.; Zhang, Y.; Yan, Y. G.; Hu, S. Q.; Zhang, J. Adsorption Mechanism of Oil Components on Water-Wet Mineral Surface: A Molecular Dynamics Simulation Study. *Energy* **2013**, *59*, 295−300.

(9) Larentzos, J. P.; Greathouse, J. A.; Cygan, R. T. An ab Initio and Classical Molecular Dynamics Investigation of the Structural and Vibrational Properties of Talc and Pyrophyllite. *J. Phys. Chem. C* **2007**, *111*, 12752−12759.

(10) Dauber-Osguthorpe, P.; Roberts, V. A.; Osguthorpe, D. J.; Wolff, J.; Genest, M.; Hagler, A. T. Structure and Energetics of Ligand Binding to Proteins: *Escherichia Coli* Dihydrofolate Reductase-Trimethoprim, a Drug-Receptor System. *Proteins: Struct., Funct., Genet.* **1988**, *4*, 31−47.

(11) Cygan, R. T.; Liang, J.-J.; Kalinichev, A. G. Molecular Models of Hydroxide, Oxyhydroxide, and Clay Phases and the Development of a General Force Field. *J. Phys. Chem. B* **2004**, *108*, 1255−1266.

(12) Brady, P. V.; Cygan, R. T.; Nagy, K. L. Molecular Controls on Kaolinite Surface Charge. *J. Colloid Interface Sci.* **1996**, *183*, 356−364.

(13) Rotenberg, B.; Marry, V.; Vuilleumier, R.; Malikova, N.; Simon, C.; Turq, P. Water and Ions in Clays: Unraveling the Interlayer/Micropore Exchange Using Molecular Dynamics. *Geochim. Cosmochim. Acta* **2007**, *71*, 5089−5101.

(14) Churakov, S. V.; Gimmi, T. Up-Scaling of Molecular Diffusion Coefficients in Clays: A Two-Step Approach. *J. Phys. Chem. C* **2011**, *115*, 6703−6714.

(15) Yu, K. A.; Schmidt, J. R. Elucidating the Crystal Face- and Hydration-Dependent Catalytic Activity of Hydrotalcites in Biodiesel Production. *J. Phys. Chem. C* **2011**, *115*, 1887−1898.

(16) Heinz, H.; Lin, T. J.; Mishra, R. K.; Emami, F. S. Thermodynamically Consistent Force Fields for the Assembly of Inorganic, Organic, and Biological Nanostructures: The INTERFACE Force Field. *Langmuir* **2013**, *29*, 1754−1765.

(17) Martins, D. M. S.; Molinari, M.; Goncalves, M. A.; Mirao, J. P.; Parker, S. C. Toward Modeling Clay Mineral Nanoparticles: The Edge

Surfaces of Pyrophyllite and Their Interaction with Water. *J. Phys. Chem. C* **2014**, *118*, 27308−27317.
(18) Zeitler, T. R.; Greathouse, J. A.; Gale, J. D.; Cygan, R. T. Vibrational Analysis of Brucite Surfaces and the Development of an Improved Force Field for Molecular Simulation of Interfaces. *J. Phys. Chem. C* **2014**, *118*, 7946−7953.
(19) Zeitler, T. R.; Greathouse, J. A.; Cygan, R. T. Effects of Thermodynamic Ensembles and Mineral Surfaces on Interfacial Water Structure. *Phys. Chem. Chem. Phys.* **2012**, *14*, 1728−1734.
(20) Sposito, G. *The Surface Chemistry of Soils*; Oxford University Press: New York, 1984.
(21) Speight, J. G. *The Chemistry and Technology of Petroleum* 5th ed.; CRC Press: Boca Raton, FL, 2007.
(22) Aitken, C. M.; Jones, D. M.; Larter, S. R. Anaerobic Hydrocarbon Biodegradation in Deep Subsurface Oil Reservoirs. *Nature* **2004**, *431*, 291−294.
(23) Lee, S. Y.; Webb, K. J.; Collins, I. R.; Lager, A.; Clarke, S. M.; O'Sullivan, M.; Routh, A. F. Low Salinity Oil Recovery: Increasing Understanding of the Underlying Mechanisms. In *SPE Improved Oil Recovery Symposium*; Society of Petroleum Engineers: Tulsa, OK, 2010; p SPE-129722-MS.
(24) Delley, B. An All-Electron Numerical-Method for Solving the Local Density Functional for Polyatomic-Molecules. *J. Chem. Phys.* **1990**, *92*, 508−517.
(25) Delley, B. From Molecules to Solids with the $DMol^3$ Approach. *J. Chem. Phys.* **2000**, *113*, 7756−7764.
(26) Perdew, J. P.; Wang, Y. Accurate and Simple Analytic Representation of the Electron-Gas Correlation-Energy. *Phys. Rev. B: Condens. Matter Mater. Phys.* **1992**, *45*, 13244−13249.
(27) Bish, D. L. Rietveld Refinement of the Kaolinite Structure at 1.5 K. *Clays Clay Miner.* **1993**, *41*, 738−744.
(28) Lee, J. H.; Guggenheim, S. Single-crystal X-ray Refinement of Pyrophyllite-1Tc. *Am. Mineral.* **1981**, *66*, 350−357.
(29) Plimpton, S. J. Fast Parallel Algorithms for Short-Range Molecular Dynamics. *J. Comput. Phys.* **1995**, *117*, 1−19.
(30) Greathouse, J. A.; Cygan, R. T. Molecular Dynamics Simulation of Uranyl(VI) Adsorption Equilibria onto an External Montmorillonite Surface. *Phys. Chem. Chem. Phys.* **2005**, *7*, 3580−3586.
(31) Greathouse, J. A.; Cygan, R. T. Water Structure and Aqueous Uranyl(VI) Adsorption Equilibria onto External Surfaces of Beidellite, Montmorillonite, and Pyrophyllite: Results from Molecular Simulations. *Environ. Sci. Technol.* **2006**, *40*, 3865−3871.
(32) Teich-McGoldrick, S. L.; Greathouse, J. A.; Cygan, R. T. Molecular Dynamics Simulations of Uranyl Adsorption and Structure on the Basal Surface of Muscovite. *Mol. Simul.* **2014**, *40*, 610−617.
(33) Greathouse, J. A.; Durkin, J. S.; Larentzos, J. P.; Cygan, R. T. Implementation of a Morse Potential to Model Hydroxyl Behavior in Phyllosilicates. *J. Chem. Phys.* **2009**, *130*, 134713.
(34) Teich-McGoldrick, S. L.; Greathouse, J. A.; Jové-Colón, C. F.; Cygan, R. T. Swelling Properties of Montmorillonite and Beidellite Clay Minerals from Molecular Simulation: Comparison of Temperature, Interlayer Cation, and Charge Location Effects. *J. Phys. Chem. C* **2015**, *119*, 20880.
(35) Teich-McGoldrick, S. L.; Greathouse, J. A.; Cygan, R. T. Molecular Dynamics Simulations of Structural and Mechanical Properties of Muscovite: Pressure and Temperature Effects. *J. Phys. Chem. C* **2012**, *116*, 15099−15107.
(36) Ockwig, N. W.; Greathouse, J. A.; Durkin, J. S.; Cygan, R. T.; Daemen, L. L.; Nenoff, T. M. Nanoconfined Water in Magnesium-Rich 2:1 Phyllosilicates. *J. Am. Chem. Soc.* **2009**, *131*, 8155−8162.
(37) Morrow, C. P.; Yazaydin, A. O.; Krishnan, M.; Bowers, G. M.; Kalinichev, A. G.; Kirkpatrick, R. J. Structure, Energetics, and Dynamics of Smectite Clay Interlayer Hydration: Molecular Dynamics and Metadynamics Investigation of Na-Hectorite. *J. Phys. Chem. C* **2013**, *117*, 5172−5187.
(38) Liu, X. D.; Lu, X. C. A Thermodynamic Understanding of Clay-Swelling Inhibition by Potassium Ions. *Angew. Chem., Int. Ed.* **2006**, *45*, 6300−6303.
(39) Ferrage, E.; Sakharov, B. A.; Michot, L. J.; Delville, A.; Bauer, A.; Lanson, B.; Grangeon, S.; Frapper, G.; Jiménez-Ruiz, M.; Cuello, G. J. Hydration Properties and Interlayer Organization of Water and Ions in Synthetic Na-Smectite with Tetrahedral Layer Charge. Part 2. Toward a Precise Coupling between Molecular Simulations and Diffraction Data. *J. Phys. Chem. C* **2011**, *115*, 1867−1881.
(40) Marry, V.; Dubois, E.; Malikova, N.; Durand-Vidal, S.; Longeville, S.; Breu, J. Water Dynamics in Hectorite Clays: Infuence of Temperature Studied by Coupling Neutron Spin Echo and Molecular Dynamics. *Environ. Sci. Technol.* **2011**, *45*, 2850−2855.
(41) Marry, V.; Turq, P. Microscopic Simulations of Interlayer Structure and Dynamics in Bihydrated Heteroionic Montmorillonites. *J. Phys. Chem. B* **2003**, *107*, 1832−1839.
(42) Greathouse, J. A.; Hart, D. B.; Bowers, G. M.; Kirkpatrick, R. J.; Cygan, R. T. Molecular Simulation of Structure and Diffusion at Smectite−Water Interfaces: Using Expanded Clay Interlayers as Model Nanopores. *J. Phys. Chem. C* **2015**, *119*, 17126−17136.
(43) Greathouse, J. A.; Hart, D. B.; Ochs, M. E. Alcohol and Thiol Adsorption on (Oxy)hydroxide and Carbon Surfaces: Molecular Dynamics Simulation and Desorption Experiments. *J. Phys. Chem. C* **2012**, *116*, 26756−26764.
(44) Churakov, S. V. Mobility of Na and Cs on Montmorillonite Surface under Partially Saturated Conditions. *Environ. Sci. Technol.* **2013**, *47*, 9816−9823.
(45) Churakov, S. V.; Gimmi, T.; Unruh, T.; Van Loon, L. R.; Juranyi, F. Resolving Diffusion in Clay Minerals at Different Time Scales: Combination of Experimental and Modeling Approaches. *Appl. Clay Sci.* **2014**, *96*, 36−44.
(46) Teleman, O.; Jonsson, B.; Engstrom, S. A Molecular Dynamics Simulation of a Water Model with Intramolecular Degrees of Freedom. *Mol. Phys.* **1987**, *60*, 193−203.
(47) Smith, D. R.; Dang, L. X. Computer Simulations of NaCl Association in Polarizable Water. *J. Chem. Phys.* **1994**, *100*, 3757−3766.
(48) Koneshan, S.; Rasaiah, J. C.; Lynden-Bell, R. M.; Lee, S. H. Solvent Structure, Dynamics, and Ion Mobility in Aqueous Solutions at 25 Degrees C. *J. Phys. Chem. B* **1998**, *102*, 4193−4204.
(49) Szczerba, M.; Kalinichev, A. G. Intercalation of Ethylene Glycol in Smectites: Several Molecular Simulation Models Verified by X-ray Diffraction Data. *Clays Clay Miner.* **2016**, *64*, 488−502.
(50) Plimpton, S. J.; Pollock, R.; Stevens, M. *Particle-Mesh Ewald and rRESPA for Parallel Molecular Dynamics Simulations*, Eighth SIAM Conference on Parallel Processing for Scientific Computing, 1997.
(51) Teter, D. M.; Cygan, R. T. *Large-Scale Molecular Dynamics Simulations of Metal Sorption onto the Basal Surfaces of Clay Minerals*; NUREG/CR-6757; Sandia National Laboratories: 2002.
(52) Greathouse, J. A.; Geatches, D. l.; Pike, D. Q.; Greenwell, H. C.; Johnston, C. T.; Wilcox, J.; Cygan, R. T. Methylene Blue Adsorption on the Basal Surfaces of Kaolinite: Structure and Thermodynamics from Quantum and Classical Molecular Simulation. *Clays Clay Miner.* **2015**, *63*, 185−198.
(53) Tunega, D.; Bucko, T.; Zaoui, A. Assessment of Ten Dft Methods in Predicting Structures of Sheet Silicates: Importance of Dispersion Corrections. *J. Chem. Phys.* **2012**, *137*, 114105.
(54) Brient, J. A.; P.J, W.; Doyle, M. N. Naphthenic Acids. In *Encyclopedia of Chemical Technology*; Kroschwitz, J. I., Ed.; John Wiley & Sons: New York, 1995; Vol. *16*, pp 1017−1029.
(55) Jiang, T. M.; Hirasaki, G. J.; Miller, C. A.; Ng, S. Wettability Alteration of Clay in Solid-Stabilized Emulsions. *Energy Fuels* **2011**, *25*, 2551−2558.

DOI: 10.1021/acs.jpcc.7b06454
J. Phys. Chem. C 2017, 121, 22773−22786

Supporting Information for:

Adsorption of Aqueous Crude Oil Components on the Basal Surfaces of Clay Minerals: Molecular Simulations Including Salinity and Temperature Effects

J. A. Greathouse,[1*] R. T. Cygan,[1] J. T. Fredrich[2], and G. R. Jerauld[2]

[1]Sandia National Laboratories, Albuquerque, New Mexico 87185-0754, USA
[2]BP America, P.O. Box 3092, Houston, Texas 77079, USA

[*]Corresponding author email address: jagreat@sandia.gov

Table S1. DFT-optimized Interatomic Distances for Gas-phase Complexes

complex	bond	*r* (Å)
Ca^{2+}-$DHNA^{-}$	Ca-O	2.14
Na^{+}-$DHNA^{-}$	Na-O	2.21

Table S2. DFT-optimized Interatomic Distances for Kaolinite Complexes

complex	bond	r (Å)
Ca^{2+}	Ca-O_{Kaol}	2.21
Na^{+}	Na-O_{Kaol}	2.26
DHNA	O_{DHNA}-H_{Kaol}	1.99
$DHNA^{-}$	O_{DHNA}-H_{Kaol}	1.70
Ca^{2+}-$DHNA^{-}$	Ca-O_{DHNA}	2.36
	Ca-O_{Kaol}	2.32
	O_{DHNA}-H_{Kaol}	1.91
Na^{+}-$DHNA^{-}$	Na-O_{DHNA}	2.39
	Na-O_{Kaol}	2.32
	O_{DHNA}-H_{Kaol}	1.88

Table S3. DFT-optimized Interatomic Distances for Pyrophyllite Complexes

complex	bond	r (Å)
Ca^{2+}	Ca-$O_{bridging}$	2.36
	Ca-O_{OH}	2.74
Na^{+}	Na-$O_{bridging}$	2.44
	Na-O_{OH}	3.35
DHNA	O_{DHNA}-$O_{bridging}$	3.09
$DHNA^{-}$	O_{DHNA}-$O_{bridging}$	2.42
Ca^{2+}-$DHNA^{-}$	Ca-O_{DHNA}	2.24
	Ca-$O_{bridging}$	2.52
	Ca-O_{OH}	3.69
Na^{+}-$DHNA^{-}$	Na-O_{DHNA}	2.26
	Na-$O_{bridging}$	2.60
	Na-O_{OH}	4.02

Table S4. DFT-optimized Interatomic Distances for Montmorillonite Complexes

complex	bond	r (Å)
Ca^{2+}	Ca-$O_{bridging}$	2.37
	Ca-O_{OH}	2.51
Na^{+}	Na-$O_{bridging}$	2.42
	Na-O_{OH}	2.98
DHNA	O_{DHNA}-$O_{bridging}$	3.28
$DHNA^{-}$	O_{DHNA}-$O_{bridging}$	2.37
Ca^{2+}-$DHNA^{-}$	Ca-O_{DHNA}	2.23
	Ca-$O_{bridging}$	2.57
	Ca-O_{OH}	3.59
Na^{+}-$DHNA^{-}$	Na-O_{DHNA}	2.23
	Na-$O_{bridging}$	2.68
	Na-O_{OH}	5.25

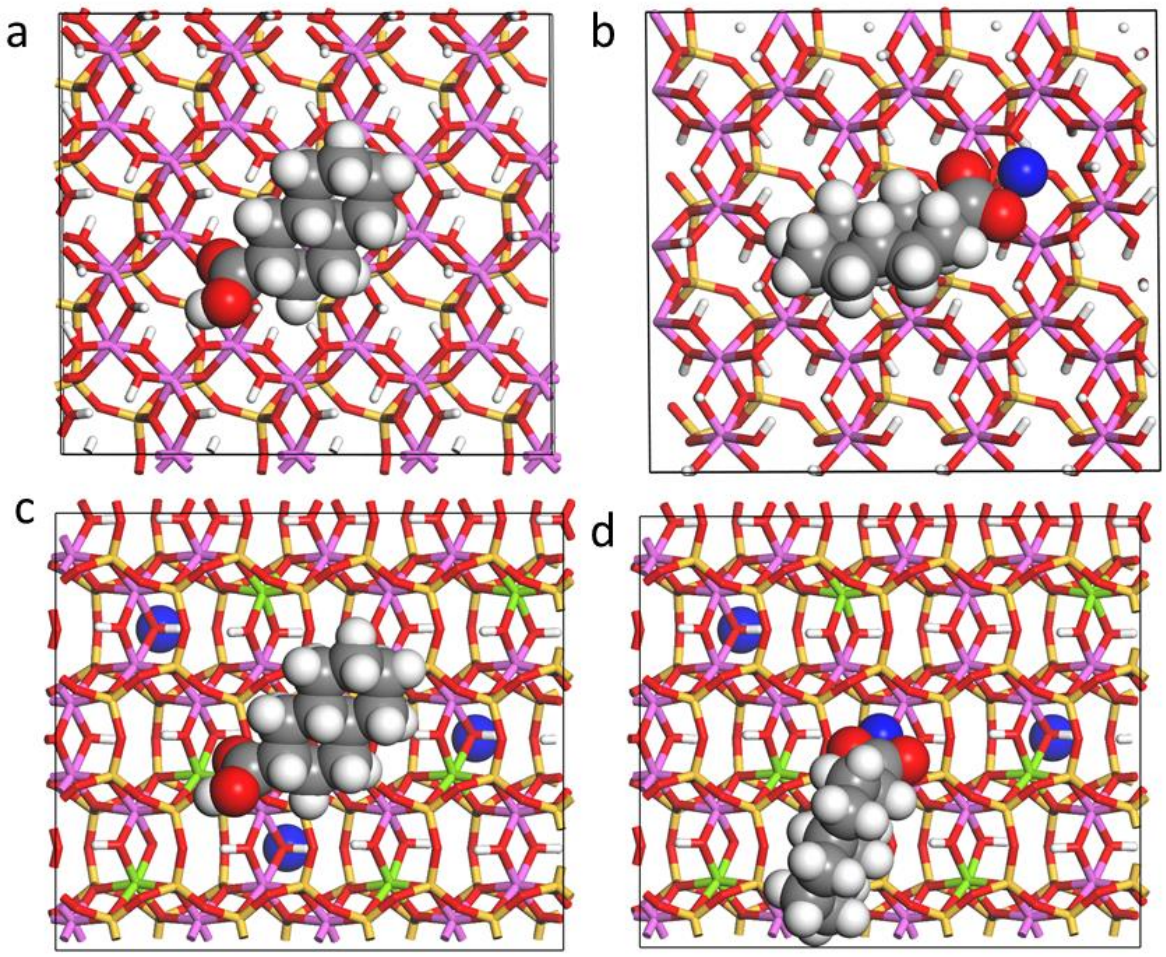

Figure S1. Top-down view of DFT-optimized structures $DHNA^-$ surface complexes from Figure 4: a) DHNA on kaolinite, b) Ca^{2+}-$DHNA^-$ on kaolinite, c) DHNA on montmorillonite, and d) Ca^{2+}-$DHNA^-$ on montmorillonite.

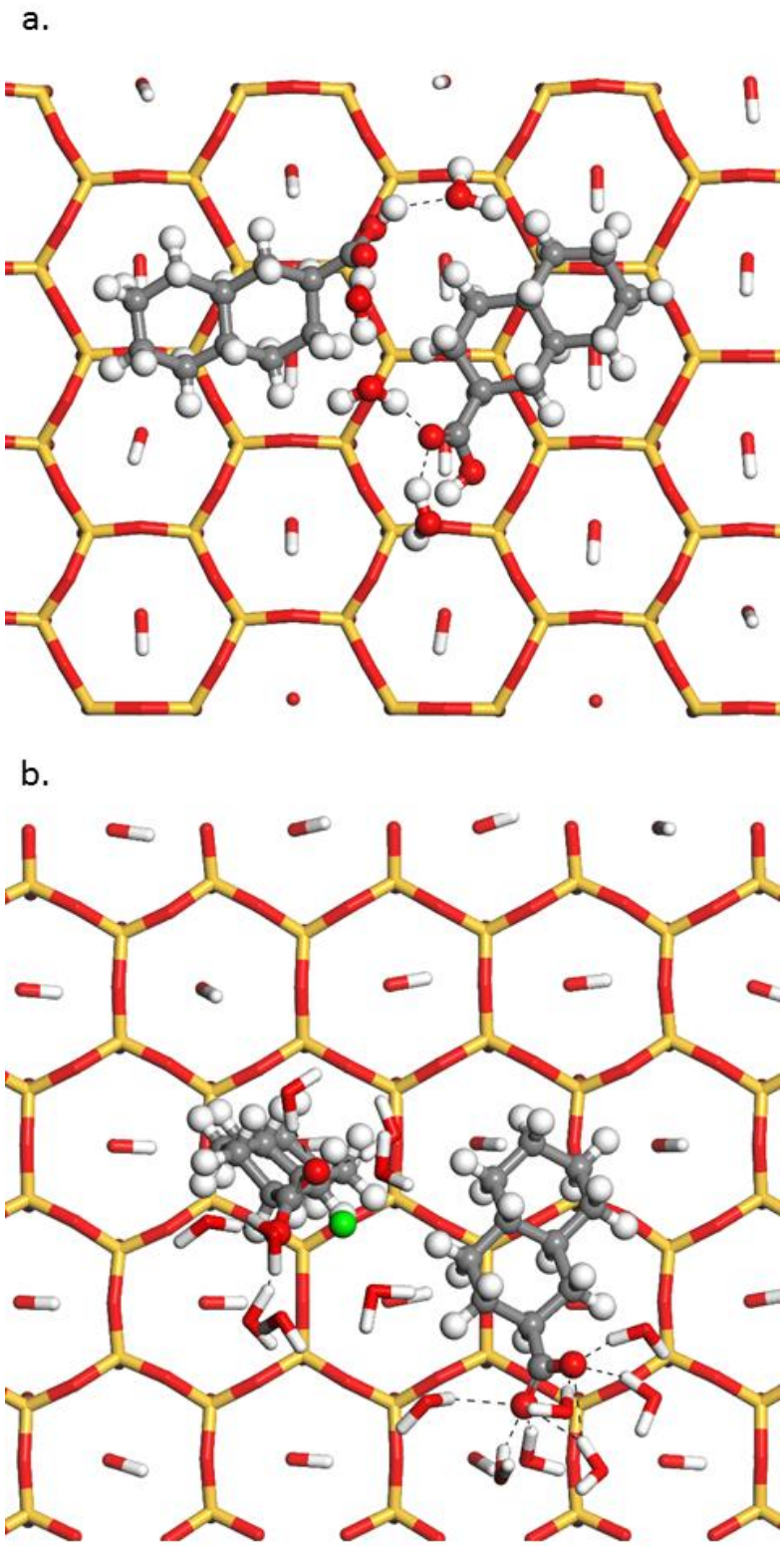

Figure S2. Top-down view of MD simulations from Figure 10, 300 K with no added $CaCl_2$ (0 ppm $CaCl_2$) showing (a) DHNA and (b) $DHNA^-$ adsorbed on the pyrophyllite surface.

LAMMPS data file for cyclohexane

18 atoms
18 bonds
36 angles
54 dihedrals
0 impropers

2 atom types
2 bond types
3 angle types
3 dihedral types

Masses

1 12.011150 # c2
2 1.007970 # h

Pair Coeffs # lj/cut/coul/long

1 0.0389999952 3.8754094636 # c2
2 0.0380000011 2.4499714540 # h

Bond Coeffs # harmonic

1 322.7158 1.5260 # c2-c2
2 340.6175 1.1050 # c2-h

Angle Coeffs # harmonic

1 46.6000 110.5000 # c2-c2-c2
2 44.4000 110.0000 # c2-c2-h
3 39.5000 106.4000 # h-c2-h

Dihedral Coeffs # harmonic

1 0.1581 1 3 # c2-c2-c2-c2
2 0.1581 1 3 # c2-c2-c2-h
3 0.1581 1 3 # h-c2-c2-h

Atoms # full

1 168 1 -0.200000 15.885925912 31.666003523 34.622380501 0 0 0 # c2
2 168 1 -0.200000 16.684128369 30.378542136 34.295069141 0 0 0 # c2
3 168 1 -0.200000 18.059950287 30.336840689 34.983901254 0 0 0 # c2
4 168 1 -0.200000 18.929177332 31.580007579 34.667031607 0 0 0 # c2
5 168 1 -0.200000 18.141129945 32.870478656 34.327195391 0 0 0 # c2
6 168 1 -0.200000 16.745339193 32.906428473 34.975913620 0 0 0 # c2
7 168 2 0.100000 15.191276683 31.469845689 35.462419327 0 0 0 # h
8 168 2 0.100000 15.230975954 31.899527244 33.760182373 0 0 0 # h
9 168 2 0.100000 16.086545635 29.486367686 34.562558418 0 0 0 # h

10	168	2	0.100000	16.831123083	30.319257771	33.198119977	0	0	0	# h
11	168	2	0.100000	18.607073760	29.415270765	34.708215600	0	0	0	# h
12	168	2	0.100000	17.910193628	30.276383518	36.080273627	0	0	0	# h
13	168	2	0.100000	19.609187974	31.352675219	33.822891824	0	0	0	# h
14	168	2	0.100000	19.598542960	31.766977822	35.529503639	0	0	0	# h
15	168	2	0.100000	18.026992492	32.938747035	33.226817334	0	0	0	# h
16	168	2	0.100000	18.730936041	33.759859164	34.619541759	0	0	0	# h
17	168	2	0.100000	16.206889893	33.830919365	34.693312810	0	0	0	# h
18	168	2	0.100000	16.863329623	32.956788039	36.076864582	0	0	0	# h

LAMMPS data file for hexane

20 atoms
19 bonds
36 angles
45 dihedrals
0 impropers

3 atom types
4 bond types
7 angle types
7 dihedral types

Masses

1 12.011150 # c3
2 12.011150 # c2
3 1.007970 # h

Pair Coeffs # lj/cut/coul/long

1 0.0389999952 3.8754094636 # c3
2 0.0389999952 3.8754094636 # c2
3 0.0380000011 2.4499714540 # h

Bond Coeffs # harmonic

1 322.7158 1.5260 # c3-c2
2 340.6175 1.1050 # c3-h
3 340.6175 1.1050 # c2-h
4 322.7158 1.5260 # c2-c2

Angle Coeffs # harmonic

1 44.4000 110.0000 # c2-c3-h
2 39.5000 106.4000 # h-c3-h
3 44.4000 110.0000 # c3-c2-h
4 46.6000 110.5000 # c3-c2-c2
5 39.5000 106.4000 # h-c2-h
6 44.4000 110.0000 # c2-c2-h
7 46.6000 110.5000 # c2-c2-c2

Dihedral Coeffs # harmonic

1 0.1581 1 3 # h-c3-c2-h
2 0.1581 1 3 # h-c3-c2-c2
3 0.1581 1 3 # c3-c2-c2-h
4 0.1581 1 3 # c3-c2-c2-c2
5 0.1581 1 3 # h-c2-c2-h
6 0.1581 1 3 # c2-c2-c2-h
7 0.1581 1 3 # c2-c2-c2-c2

Atoms # full

1	1	1	-0.300000	12.490909655	12.010064840	42.595691764	0	0	0 # c3
2	1	2	-0.200000	13.767408940	11.169814887	42.573664717	0	0	0 # c2
3	1	3	0.100000	11.588747813	11.371335031	42.580690605	0	0	0 # h
4	1	3	0.100000	12.421277705	12.684359252	41.721600366	0	0	0 # h
5	1	3	0.100000	12.424337090	12.639925281	43.501841024	0	0	0 # h
6	1	3	0.100000	13.769326263	10.523552397	41.673509376	0	0	0 # h
7	1	3	0.100000	13.771310064	10.479371010	43.440469444	0	0	0 # h
8	1	2	-0.200000	15.023911055	12.052548565	42.594628821	0	0	0 # c2
9	1	3	0.100000	15.014142113	12.697295877	43.496148045	0	0	0 # h
10	1	3	0.100000	15.012451882	12.743155097	41.728136749	0	0	0 # h
11	1	2	-0.200000	16.309517050	11.207911639	42.570778369	0	0	0 # c2
12	1	3	0.100000	16.317749654	10.563134725	41.669517212	0	0	0 # h
13	1	3	0.100000	16.321995019	10.516856838	43.437158907	0	0	0 # h
14	1	2	-0.200000	17.566338011	12.090260887	42.592771416	0	0	0 # c2
15	1	3	0.100000	17.563545951	12.736827681	43.492657579	0	0	0 # h
16	1	3	0.100000	17.563800116	12.781960206	41.726911682	0	0	0 # h
17	1	1	-0.300000	18.842520066	11.249561943	42.571022764	0	0	0 # c3
18	1	3	0.100000	18.911090522	10.620123043	41.664343906	0	0	0 # h
19	1	3	0.100000	18.912263711	10.574663723	43.444347972	0	0	0 # h
20	1	3	0.100000	19.744528498	11.888483325	42.585872539	0	0	0 # h

LAMMPS data file for toluene

15 atoms
15 bonds
24 angles
30 dihedrals
6 impropers

3 atom types
4 bond types
5 angle types
6 dihedral types
2 improper types

Masses

1 12.011150 # cp
2 12.011150 # c3
3 1.007970 # h

Pair Coeffs # lj/cut/coul/long

1 0.1479999981 3.6170487995 # cp
2 0.0389999952 3.8754094636 # c3
3 0.0380000011 2.4499714540 # h

Bond Coeffs # harmonic

1 480.0000 1.3400 # cp-cp
2 363.4164 1.0800 # cp-h
3 283.0924 1.5100 # cp-c3
4 340.6175 1.1050 # c3-h

Angle Coeffs # harmonic

1 90.0000 120.0000 # cp-cp-cp
2 37.0000 120.0000 # cp-cp-h
3 44.2000 120.0000 # cp-cp-c3
4 44.4000 110.0000 # cp-c3-h
5 39.5000 106.4000 # h-c3-h

Dihedral Coeffs # harmonic

1 3.0000 -1 2 # cp-cp-cp-cp
2 3.0000 -1 2 # cp-cp-cp-h
3 3.0000 -1 2 # h-cp-cp-h
4 3.0000 -1 2 # cp-cp-cp-c3
5 3.0000 -1 2 # c3-cp-cp-h
6 0.0000 1 2 # cp-cp-c3-h

Improper Coeffs # cvff

```
   1    0.3700  -1   2 # cp-cp-cp-h
   2    0.3700  -1   2 # cp-cp-cp-c3

Atoms # full

    1   1692   1 -0.100000    19.737612641    13.280434687    45.526476956   0   0   0 # cp
    2   1692   1 -0.100000    19.189397260    12.003954645    45.638801933   0   0   0 # cp
    3   1692   1 -0.100000    20.020935841    10.900690024    45.825575698   0   0   0 # cp
    4   1692   1 -0.100000    21.405579689    11.075314623    45.900496112   0   0   0 # cp
    5   1692   1  0.000000    21.968776252    12.354149942    45.792253776   0   0   0 # cp
    6   1692   1 -0.100000    21.122147503    13.454355572    45.601347086   0   0   0 # cp
    7   1692   2 -0.300000    23.473608645    12.541849876    45.861147103   0   0   0 # c3
    8   1692   3  0.100000    19.094173753    14.139252128    45.379556166   0   0   0 # h
    9   1692   3  0.100000    18.116320489    11.869467860    45.580297489   0   0   0 # h
   10   1692   3  0.100000    19.595880231     9.908061834    45.911546854   0   0   0 # h
   11   1692   3  0.100000    22.041347071    10.209449229    46.042031542   0   0   0 # h
   12   1692   3  0.100000    21.533568932    14.452133672    45.507726514   0   0   0 # h
   13   1692   3  0.100000    23.929979605    12.460108422    44.858311413   0   0   0 # h
   14   1692   3  0.100000    23.960905686    11.786789600    46.504529490   0   0   0 # h
   15   1692   3  0.100000    23.754994812    13.529427620    46.269770863   0   0   0 # h
```

LAMMPS data file for DHNA

31 atoms
32 bonds
64 angles
107 dihedrals
1 impropers

7 atom types
9 bond types
16 angle types
27 dihedral types
1 improper types

Masses

1 1.007970 # h
2 12.011150 # c2
3 12.011150 # c1
4 12.011150 # c'
5 15.999400 # o'
6 15.999400 # oh
7 1.007970 # ho

Pair Coeffs # lj/cut/coul/long

1 0.0380000011 2.4499714540 # h
2 0.0389999952 3.8754094636 # c2
3 0.0389999952 3.8754094636 # c1
4 0.1479999981 3.6170487995 # c'
5 0.2280000124 2.8597848722 # o'
6 0.1554164124 3.1655200879 # oh
7 0.0000000000 0.0000000000 # ho

Bond Coeffs # harmonic

1 340.6175 1.1050 # h-c2
2 322.7158 1.5260 # c2-c2
3 322.7158 1.5260 # c2-c1
4 322.7158 1.5260 # c1-c1
5 340.6175 1.1050 # h-c1
6 283.0924 1.5200 # c1-c'
7 615.3220 1.2300 # c'-o'
8 400.0000 1.3700 # c'-oh
9 540.6336 0.9600 # oh-ho

Angle Coeffs # harmonic

1 44.4000 110.0000 # h-c2-c2
2 39.5000 106.4000 # h-c2-h

```
 3    46.6000   110.5000 # c2-c2-c2
 4    46.6000   110.5000 # c2-c2-c1
 5    44.4000   110.0000 # h-c2-c1
 6    46.6000   110.5000 # c2-c1-c2
 7    46.6000   110.5000 # c2-c1-c1
 8    44.4000   110.0000 # h-c1-c2
 9    44.4000   110.0000 # h-c1-c1
10    46.6000   110.5000 # c1-c2-c1
11    46.6000   110.5000 # c2-c1-c'
12    45.0000   109.5000 # h-c1-c'
13    68.0000   120.0000 # c1-c'-o'
14   122.8000   110.0000 # c1-c'-oh
15   145.0000   123.0000 # o'-c'-oh
16    50.0000   112.0000 # c'-oh-ho
```

Dihedral Coeffs # harmonic

```
 1    0.1581   1   3 # h-c2-c2-c1
 2    0.1581   1   3 # h-c2-c2-h
 3    0.1581   1   3 # c2-c2-c2-c1
 4    0.1581   1   3 # h-c2-c2-c2
 5    0.1581   1   3 # c2-c2-c2-c2
 6    0.1581   1   3 # c2-c2-c1-c2
 7    0.1581   1   3 # c2-c2-c1-c1
 8    0.1581   1   3 # c2-c2-c1-h
 9    0.1581   1   3 # h-c2-c1-c2
10    0.1581   1   3 # h-c2-c1-c1
11    0.1581   1   3 # h-c2-c1-h
12    0.1581   1   3 # c1-c2-c1-c2
13    0.1581   1   3 # c1-c2-c1-c1
14    0.1581   1   3 # c1-c2-c1-h
15    0.1581   1   3 # c2-c1-c1-c2
16    0.1581   1   3 # h-c1-c1-c2
17    0.1581   1   3 # h-c1-c1-h
18    0.1581   1   3 # c1-c2-c1-c'
19    0.1581   1   3 # h-c2-c1-c'
20    0.1581   1   3 # c2-c2-c1-c'
21    0.0000   1   0 # c2-c1-c'-o'
22    0.0000   1   0 # c2-c1-c'-oh
23    0.0000   1   0 # h-c1-c'-o'
24    0.0000   1   0 # h-c1-c'-oh
25    0.1581   1   3 # c1-c2-c2-c1
26    2.2500  -1   2 # c1-c'-oh-ho
27    2.2500  -1   2 # o'-c'-oh-ho
```

Improper Coeffs # cvff

```
 1   11.6000  -1   2 # c1-c'-o'-oh
```

Atoms # full

1	1	1	0.100000	7.631240308	23.654968800	42.569516848	0	0	0 # h
2	1	2	-0.200000	8.704844913	23.413244101	42.405298742	0	0	0 # c2
3	1	2	-0.200000	9.538373595	24.315123752	43.347010946	0	0	0 # c2
4	1	2	-0.200000	11.131989659	24.280363744	43.137813080	0	0	0 # c2
5	1	3	-0.100000	11.444349037	24.521835670	41.605928236	0	0	0 # c1
6	1	3	-0.100000	10.667581385	23.587822367	40.712606586	0	0	0 # c1
7	1	2	-0.200000	9.165351499	23.676941597	40.923283518	0	0	0 # c2
8	1	1	0.100000	9.306958044	24.046618058	44.373101558	0	0	0 # h
9	1	1	0.100000	11.524298623	23.295376517	43.424060142	0	0	0 # h
10	1	1	0.100000	8.885247537	24.752930353	40.673475781	0	0	0 # h
11	1	2	-0.200000	12.945429625	24.479572360	41.292477006	0	0	0 # c2
12	1	3	-0.100000	13.329316145	24.707846301	39.762991291	0	0	0 # c1
13	1	2	-0.200000	12.525809440	23.756787993	38.913153429	0	0	0 # c2
14	1	2	-0.200000	10.984938637	23.763398379	39.187265746	0	0	0 # c2
15	1	1	0.100000	13.316424836	23.457516969	41.523300346	0	0	0 # h
16	1	4	0.410000	14.813543306	24.791607363	39.335416441	0	0	0 # c'
17	1	1	0.100000	12.924309329	22.765899395	39.032731548	0	0	0 # h
18	1	1	0.100000	10.440787389	24.587741812	38.646058659	0	0	0 # h
19	1	5	-0.380000	15.648316159	24.038480013	39.851955660	0	0	0 # o'
20	1	6	-0.380000	15.028852634	25.550155744	38.221736186	0	0	0 # oh
21	1	1	0.100000	8.947871940	22.306144060	42.670187618	0	0	0 # h
22	1	1	0.100000	9.194564408	25.352395197	43.249495590	0	0	0 # h
23	1	1	0.100000	11.629319276	24.930650321	43.817098058	0	0	0 # h
24	1	1	0.100000	11.095267738	25.552501425	41.517952248	0	0	0 # h
25	1	1	0.100000	11.010973190	22.585679496	41.000166300	0	0	0 # h
26	1	1	0.100000	8.614927526	22.938734625	40.280851910	0	0	0 # h
27	1	1	0.100000	13.572983686	25.070590751	41.934088315	0	0	0 # h
28	1	1	0.100000	12.946960026	25.691870484	39.516908749	0	0	0 # h
29	1	1	0.100000	12.569378433	24.005969733	37.807409338	0	0	0 # h
30	1	1	0.100000	10.541911215	22.813077479	38.712646181	0	0	0 # h
31	1	7	0.350000	15.895212912	25.243286520	37.753869144	0	0	0 # ho

LAMMPS data file for DHNA_anion

30 atoms
31 bonds
63 angles
105 dihedrals
1 impropers

5 atom types
7 bond types
14 angle types
23 dihedral types
1 improper types

Masses

1 1.007970 # h
2 12.011150 # c2
3 12.011150 # c1
4 12.011150 # c-
5 15.999400 # o-

Pair Coeffs # lj/cut/coul/long

1 0.0380000011 2.4499714540 # h
2 0.0389999952 3.8754094636 # c2
3 0.0389999952 3.8754094636 # c1
4 0.1479999981 3.6170487995 # c-
5 0.2280000124 2.8597848722 # o-

Bond Coeffs # harmonic

1 340.6175 1.1050 # h-c2
2 322.7158 1.5260 # c2-c2
3 322.7158 1.5260 # c2-c1
4 322.7158 1.5260 # c1-c1
5 340.6175 1.1050 # h-c1
6 283.0924 1.5200 # c1-c-
7 540.0000 1.2500 # c--o-

Angle Coeffs # harmonic

1 44.4000 110.0000 # h-c2-c2
2 39.5000 106.4000 # h-c2-h
3 46.6000 110.5000 # c2-c2-c2
4 46.6000 110.5000 # c2-c2-c1
5 44.4000 110.0000 # h-c2-c1
6 46.6000 110.5000 # c2-c1-c2
7 46.6000 110.5000 # c2-c1-c1
8 44.4000 110.0000 # h-c1-c2
9 44.4000 110.0000 # h-c1-c1

```
 10    46.6000   110.5000 # c1-c2-c1
 11    46.6000   110.5000 # c2-c1-c-
 12    45.0000   109.5000 # h-c1-c-
 13    68.0000   120.0000 # c1-c--o-
 14   145.0000   123.0000 # o--c--o-

Dihedral Coeffs # harmonic

 1    0.1581   1   3 # h-c2-c2-c1
 2    0.1581   1   3 # h-c2-c2-h
 3    0.1581   1   3 # c2-c2-c2-c1
 4    0.1581   1   3 # h-c2-c2-c2
 5    0.1581   1   3 # c2-c2-c2-c2
 6    0.1581   1   3 # c2-c2-c1-c2
 7    0.1581   1   3 # c2-c2-c1-c1
 8    0.1581   1   3 # c2-c2-c1-h
 9    0.1581   1   3 # h-c2-c1-c2
 10    0.1581   1   3 # h-c2-c1-c1
 11    0.1581   1   3 # h-c2-c1-h
 12    0.1581   1   3 # c1-c2-c1-c2
 13    0.1581   1   3 # c1-c2-c1-c1
 14    0.1581   1   3 # c1-c2-c1-h
 15    0.1581   1   3 # c2-c1-c1-c2
 16    0.1581   1   3 # h-c1-c1-c2
 17    0.1581   1   3 # h-c1-c1-h
 18    0.1581   1   3 # c1-c2-c1-c-
 19    0.1581   1   3 # h-c2-c1-c-
 20    0.1581   1   3 # c2-c2-c1-c-
 21    0.0000   1   0 # c2-c1-c--o-
 22    0.0000   1   0 # h-c1-c--o-
 23    0.1581   1   3 # c1-c2-c2-c1

Improper Coeffs # cvff

   1   11.6000  -1   2 # c1-c--o--o-

Atoms # full

     1     1   1  0.100000     7.631240308    23.654968800    42.569516848   0   0   0 # h
     2     1   2 -0.200000     8.704844913    23.413244101    42.405298742   0   0   0 # c2
     3     1   2 -0.200000     9.538373595    24.315123752    43.347010946   0   0   0 # c2
     4     1   2 -0.200000    11.131989659    24.280363744    43.137813080   0   0   0 # c2
     5     1   3 -0.100000    11.444349037    24.521835670    41.605928236   0   0   0 # c1
     6     1   3 -0.100000    10.667581385    23.587822367    40.712606586   0   0   0 # c1
     7     1   2 -0.200000     9.165351499    23.676941597    40.923283518   0   0   0 # c2
     8     1   1  0.100000     9.306958044    24.046618058    44.373101558   0   0   0 # h
     9     1   1  0.100000    11.524298623    23.295376517    43.424060142   0   0   0 # h
    10     1   1  0.100000     8.885247537    24.752930353    40.673475781   0   0   0 # h
    11     1   2 -0.200000    12.945429625    24.479572360    41.292477006   0   0   0 # c2
    12     1   3 -0.100000    13.329316145    24.707846301    39.762991291   0   0   0 # c1
    13     1   2 -0.200000    12.525809440    23.756787993    38.913153429   0   0   0 # c2
```

14	1	2	-0.200000	10.984938637	23.763398379	39.187265746	0	0	0 # c2
15	1	1	0.100000	13.316424836	23.457516969	41.523300346	0	0	0 # h
16	1	4	0.140000	14.813543306	24.791607363	39.335416441	0	0	0 # c-
17	1	1	0.100000	12.924309329	22.765899395	39.032731548	0	0	0 # h
18	1	1	0.100000	10.440787389	24.587741812	38.646058659	0	0	0 # h
19	1	5	-0.570000	15.648316159	24.038480013	39.851955660	0	0	0 # o-
20	1	5	-0.570000	15.028852634	25.550155744	38.221736186	0	0	0 # o-
21	1	1	0.100000	8.947871940	22.306144060	42.670187618	0	0	0 # h
22	1	1	0.100000	9.194564408	25.352395197	43.249495590	0	0	0 # h
23	1	1	0.100000	11.629319276	24.930650321	43.817098058	0	0	0 # h
24	1	1	0.100000	11.095267738	25.552501425	41.517952248	0	0	0 # h
25	1	1	0.100000	11.010973190	22.585679496	41.000166300	0	0	0 # h
26	1	1	0.100000	8.614927526	22.938734625	40.280851910	0	0	0 # h
27	1	1	0.100000	13.572983686	25.070590751	41.934088315	0	0	0 # h
28	1	1	0.100000	12.946960026	25.691870484	39.516908749	0	0	0 # h
29	1	1	0.100000	12.569378433	24.005969733	37.807409338	0	0	0 # h
30	1	1	0.100000	10.541911215	22.813077479	38.712646181	0	0	0 # h